Classical model of spontaneous parametric down-conversion

Girish Kulkarni [1,*] Jeremy Rioux,[1] Boris Braverman [1,†] Maria V. Chekhova [2,3] and Robert W. Boyd[1,4]

[1]*Department of Physics, University of Ottawa, Ottawa, Ontario K1N 6N5, Canada*
[2]*Max Planck Institute for the Science of Light, Staudtstr. 2, 91058 Erlangen, Germany*
[3]*Universität Erlangen-Nürnberg, Staudtstr. 7/B2, 91058 Erlangen, Germany*
[4]*The Institute of Optics, University of Rochester, Rochester, New York 14627, USA*

We model spontaneous parametric down-conversion (SPDC) as classical difference frequency generation (DFG) of the pump field and a hypothetical stochastic "vacuum" seed field. We analytically show that the second-order spatiotemporal correlations of the field generated from the DFG process replicate those of the signal field from SPDC. Specifically, for low gain, the model is consistent with the quantum calculation of the signal photon's reduced density matrix; and for high gain, the model's predictions are in good agreement with our experimental measurements of the far-field intensity profile, orbital angular momentum spectrum, and wavelength spectrum of the SPDC field for increasing pump strengths. We further theoretically show that the model successfully captures second-order SU(1,1) interference and induced coherence effects in both gain regimes. Intriguingly, the model also correctly predicts the linear scaling of the interference visibility with object transmittance in the low-gain regime—a feature that is often regarded as a quintessential signature of the nonclassicality of induced coherence. Our model may not only lead to fundamental insights into the classical-quantum divide in the context of SPDC and induced coherence, but can also be a useful theoretical tool for numerous experiments and applications based on SPDC.

I. INTRODUCTION

Spontaneous parametric down-conversion (SPDC) is a nonlinear optical phenomenon in which an incident field known as the pump interacts with a noncentrosymmetric medium to produce a pair of fields known as signal and idler [1–3]. In the quantum paradigm, this interaction can be modeled as a series of infinitely-many contributing processes, where the nth order contribution physically corresponds to n pump photons being annihilated to produce n signal photons and n idler photons [4]. The strength of the interaction, referred to as the gain, is directly proportional to the pump field strength [5]. For typical continuous-wave and low-power pulsed pump lasers, the interaction is weak and can be approximated by the dominant first-order contribution alone, which yields an entangled two-photon signal-idler state [6–8]. In this low-gain regime, which is characterized by a linear growth of the generated fields with respect to the pump amplitude, SPDC sources are ubiquitously employed in fundamental quantum optics experiments [9–12] and optical quantum tech-

nologies [13–15]. On the other hand, for high-power pulsed pump lasers, the interaction can be strong and may comprise of significant higher-order contributions, thereby producing a bright multiphoton entangled state of the signal and idler fields [16,17]. In this high-gain regime, which is characterized by an exponential growth of the generated fields with respect to the pump amplitude, SPDC has significant potential for applications such as sub-shot noise imaging [18,19] and generation of nonclassical states of light [20,21].

While the precise form of two-photon state produced in the perturbative low-gain regime has long been analytically derived for a general pump profile [6–8], the theoretical characterization of the nonperturbative high-gain regime has proved to be much more difficult. In order to correctly evaluate higher-order contributions, one must account for the fact that the interaction Hamiltonian may not commute with itself at different times, and consequently, the Schrödinger time-evolution operator must strictly be expanded in terms of the time-ordered Dyson series instead of the usual Taylor series [22]. However, it was shown that any finite-order truncation of the Dyson series destroys the Gaussian character of the output state [23], whereas the exact solution can be proved to be a Gaussian state solely from the quadratic form of the interaction Hamiltonian [24]. Such issues can be avoided by turning to the Heisenberg picture, where one instead obtains a set of coupled differential equations for the evolution of the signal and idler mode operators [5,25–27]. However, these equations have so far been exactly solved only for the special case of a monochromatic plane-wave pump [5], and approximately solved for the cases of a broadband pump with a single spatial mode [25], and a pump with narrow spectral and

angular bandwidths [16]. Some studies have explored analytical ansatz solutions that assume gain-independent Schmidt modes for the output state [28,29]. However, these solutions have limited applicability as they are unable to account for experimental observations such as broadening of the angular spectrum and wavelength spectrum of the SPDC field with increasing gain [30,31]. More recently, a quantum calculation using the Wigner functional approach that includes the spatiotemporal and photon number degrees of freedom has been reported, but a comparison to experiment is still pending [32,33]. Thus, the theoretical characterization of high-gain SPDC still remains an active research area.

In view of the aforementioned challenges encountered in performing a general quantum calculation, one can instead ask: Is there a *classical* analytical model that can consistently predict at least a restricted class of correlations in high-gain SPDC? For instance, in the low-gain regime, it is known that second-order (in fields) autocorrelations of the individual fields can be modeled classically [34–38]. A simple and elegant approach in this context was developed in Ref. [34], where SPDC is modeled as the paraxial propagation of a classical partially-coherent source created in the nonlinear medium by the coupling of the pump field to a classical noise field that simulates the vacuum fluctuations. The second-order correlations derived using this approach were demonstrated to be consistent with the quantum calculation of the reduced one-photon density matrix in the low-gain regime. However, this approach does not appear to admit a straightforward generalization to the high-gain regime as the generated field is *a priori* assumed to scale linearly with the pump amplitude. Another approach, which has also been neatly summarized in Ref. [34], is to model SPDC as a three-wave mixing process between the pump and the vacuum fluctuations [35–37]. In particular, the spatial and spectral profiles of the SPDC field can be derived by solving differential equations involving a stochastic term that represents the vacuum fluctuations [36,37], although the origin of coherence is less clear and has been attributed to various specific experimental conditions [39,40]. However, to our knowledge, this latter approach has not been taken beyond the plane-wave pump case in the high-gain regime to derive analytical solutions for realistic pump fields with finite spectral and angular bandwidths. Moreover, this latter approach has also not yet been employed for analyzing two-crystal settings such as SU(1,1) interferometers [41,42] and induced coherence-related experiments [11,43].

In this paper, we adopt the aforementioned latter approach and model SPDC as classical difference frequency generation (DFG) of the pump field and a classical stochastic seed field that simulates the zero-point vacuum fluctuations. In contrast with previous studies, we derive analytical expressions for the second-order spatiotemporal correlations of the generated signal field for a narrow-but-finite-bandwidth pump in low- and high-gain regimes. The paper is organized as follows: In Sec. II, we set up the model and derive the second-order spatiotemporal correlation function of the generated field in low- and high-gain regimes. In Sec. III, we perform experimental measurements of the far-field intensity profile, orbital angular momentum spectrum, and wavelength spectrum for increasing pump strengths and demonstrate their agreement with the model's predictions. In Sec. IV, we extend the model
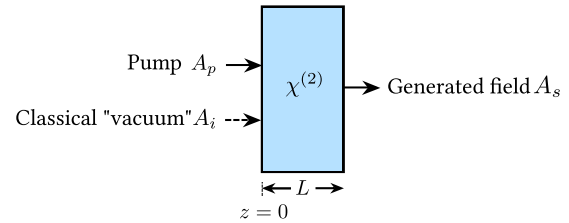

FIG. 1. Modeling SPDC as DFG of the pump with a hypothetical classical "vacuum" seed field.

to analyze SU(1,1) interference and induced coherence effects in both low- and high-gain regimes. In Sec. V, we conclude with a summary and outlook.

II. THEORETICAL MODEL

As depicted in Fig. 1, we model SPDC as DFG of the pump field A_p with a hypothetical classical seed field A_i that mimics the effect of zero-point vacuum fluctuations. Our goal is to compute the second-order spatiotemporal correlations of the generated field A_s, which is assumed to be totally absent prior to the interaction. We approximate the fields to be paraxially propagating along the longitudinal z axis. A crystal of length L and second-order nonlinear susceptibility $\chi^{(2)}$ is placed perpendicular to the z axis, and the crystal's input face is used to define $z = 0$. The Fourier amplitudes (not including propagation phases) for the pump field, classical "vacuum", and the generated fields are denoted by stochastic functions $A_j(\boldsymbol{q}_j, \omega_j, z)$, where $\boldsymbol{q}_j$ and ω_j are the transverse wavevector and frequency coordinates, for $j = p, i$, and s, respectively. In terms of the position vector $\boldsymbol{r} \equiv (\boldsymbol{\rho}, z)$, where $\boldsymbol{\rho}$ is transverse position, and wavevectors $\boldsymbol{k}_j \equiv (\boldsymbol{q}_j, k_{jz})$, we define the electric field mode functions

$$\boldsymbol{E}_j(\boldsymbol{r}, \omega_j) = \int d\boldsymbol{q}_j A_j(\boldsymbol{q}_j, \omega_j, z) \, e^{i(\boldsymbol{q}_j \cdot \boldsymbol{\rho} + k_{jz} z)}. \quad (1)$$

We now assume that the energy depletion of the pump due to the nonlinear interaction is negligible, and consequently, the pump amplitude $A_p(\boldsymbol{q}_p, \omega_p)$ is independent of z. We emphasize that the pump field can be pulsed or continuous-wave with any arbitrary spectral and spatial profile. The evolution of the other two fields is governed by the wave equation of nonlinear optics (see Eq. 2.1.23 of Ref. [3])

$$\nabla^2 \boldsymbol{E}_j(\boldsymbol{r}, \omega_j) + \frac{n_j^2 \omega_j^2}{c^2} \boldsymbol{E}_j(\boldsymbol{r}, \omega_j) = -\frac{\omega_j^2}{\epsilon_0 c^2} \boldsymbol{P}_{NL}(\boldsymbol{r}, \omega_j), \quad (2)$$

where $j = s, i$, and n_j is the refractive index inside the crystal. Assuming energy conservation, i.e., $\omega_p = \omega_s + \omega_i$, the nonlinear polarization $\boldsymbol{P}_{NL}(\boldsymbol{r}, \omega_j)$ can be written as (see Eq. 1.5.30 of Ref. [3])

$$\boldsymbol{P}_{NL}(\boldsymbol{r}, \omega_j) = 4\epsilon_0 d_{\text{eff}} \int d\omega_p \, \boldsymbol{E}_p(\boldsymbol{r}, \omega_p) \boldsymbol{E}_l^*(\boldsymbol{r}, \omega_l), \quad (3)$$

where $j = s(i)$ and $l = i(s)$. In our scalar treatment, the quantity $d_{\text{eff}} = \chi^{(2)}/2$ is the nonlinear coupling coefficient of the crystal medium, and its dependence on frequency has been ignored. Substituting Eqs. (1) and (3) into (2) and making the slowly-varying envelope approximation $\frac{\partial^2}{\partial z^2} A_j(\boldsymbol{q}_j, \omega_j, z) \ll$

$k_{jz}\frac{\partial}{\partial z}A_j(\boldsymbol{q}_j,\omega_j,z)$ for $j=s,i$, we obtain (see Appendix A for the detailed calculation)

$$\frac{\partial A_s(\boldsymbol{q}_s,\omega_s,z)}{\partial z} = \frac{2id_{\text{eff}}\omega_s^2}{k_{sz}c^2}\iint d\omega_i\,d\boldsymbol{q}_i\,A_p(\boldsymbol{q}_p,\omega_p)$$
$$\times A_i^*(\boldsymbol{q}_i,\omega_i,z)e^{i\Delta k_z z}, \quad (4a)$$

$$\frac{\partial A_i^*(\boldsymbol{q}_i,\omega_i,z)}{\partial z} = \frac{-2id_{\text{eff}}\omega_i^2}{k_{iz}c^2}\iint d\omega_s\,d\boldsymbol{q}_s\,A_p^*(\boldsymbol{q}_p,\omega_p)$$
$$\times A_s(\boldsymbol{q}_s,\omega_s,z)e^{-i\Delta k_z z}, \quad (4b)$$

where $\Delta k_z = k_{pz}-k_{sz}-k_{iz}$ is the longitudinal phase mismatch, and its dependence on $\boldsymbol{q}_s$, $\boldsymbol{q}_i$, ω_s, and ω_i has been suppressed for brevity. We have assumed that the transverse dimensions of the crystal are much larger than those of the pump beam, which leads to conservation of transverse momentum, i.e., $\boldsymbol{q}_p = \boldsymbol{q}_s + \boldsymbol{q}_i$. The above coupled differential equations (4) describe the nonlinear interaction for arbitrary strengths of the pump field.

A. Low-gain regime

When the pump power is low, the nonlinear interaction is weak. In the context of DFG with monochromatic plane waves, it is known that under weak interaction, the longitudinal growth of the seed field is negligible (see Sec. 2.8 of Ref. [3]). Hence, we approximate $A_i^*(\boldsymbol{q}_i,\omega_i,z) \approx A_i^*(\boldsymbol{q}_i,\omega_i,0)$ and simply integrate Eq. (4a) from $z=0$ to $z=L$ to obtain

$$A_s(\boldsymbol{q}_s,\omega_s,L) = \frac{2id_{\text{eff}}\omega_s^2}{k_{sz}c^2}\iint d\omega_i\,d\boldsymbol{q}_i\,A_p(\boldsymbol{q}_p,\omega_p)$$
$$\times A_i^*(\boldsymbol{q}_i,\omega_i,0)\int_0^L dz\,e^{i\Delta k_z z}$$
$$= \frac{d_{\text{eff}}L\omega_s^2}{k_{sz}c^2}\iint d\omega_i\,d\boldsymbol{q}_i\,A_p(\boldsymbol{q}_p,\omega_p)A_i^*(\boldsymbol{q}_i,\omega_i,0)$$
$$\times \text{sinc}(\Delta k_z L/2)\exp(i\Delta k_z L/2), \quad (5)$$

where $\text{sinc}(x)\equiv(\sin x)/x$. Using the above equation, we evaluate the second-order correlation function [44]

$$\langle A_s(\boldsymbol{q}_s,\omega_s,L)A_s^*(\boldsymbol{q}'_s,\omega'_s,L)\rangle$$
$$= \frac{d_{\text{eff}}^2 L^2\omega_s^2\omega_s'^2}{k_{sz}k'_{sz}c^4}\iiiint d\omega_i\,d\boldsymbol{q}_i$$
$$\times d\omega'_i\,d\boldsymbol{q}'_i\,\langle A_p(\boldsymbol{q}_s+\boldsymbol{q}_i,\omega_s+\omega_i)A_p^*(\boldsymbol{q}'_s+\boldsymbol{q}'_i,\omega'_s+\omega'_i)\rangle$$
$$\times \langle A_i(\boldsymbol{q}'_i,\omega'_i,0)A_i^*(\boldsymbol{q}_i,\omega_i,0)\rangle\,\text{sinc}(\Delta k_z L/2)$$
$$\times \text{sinc}(\Delta k'_z L/2)\,e^{i(\Delta k_z-\Delta k'_z)L/2}, \quad (6)$$

where $\langle\cdots\rangle$ denotes an ensemble average and $\Delta k'_z$ is the phase mismatch evaluated for the primed variables. We have assumed that the pump and classical "vacuum" fields have no mutual correlation, and as a result, their individual correlation functions factor out separately.

In order to evaluate the above Eq. (6), we must now substitute for $\langle A_i(\boldsymbol{q}'_i,\omega'_i,0)A_i^*(\boldsymbol{q}_i,\omega_i,0)\rangle$. While it may seem reasonable to assume that different modes of the classical "vacuum" are completely uncorrelated, i.e., $\langle A_i(\boldsymbol{q}'_i,\omega'_i,0)A_i^*(\boldsymbol{q}_i,\omega_i,0)\rangle = C\,\delta(\boldsymbol{q}_i-\boldsymbol{q}'_i)\delta(\omega_i-\omega'_i)$, it is possible to explicitly derive this relation along with the value of

the scaling factor C if we make a short detour to quantum theory. We note from the quantized theory of the electromagnetic field that (see Sec. 2.3.3 of Ref. [45])

$$\hat{\boldsymbol{E}}_i(\boldsymbol{r},\omega_i) = i\int d\boldsymbol{q}_i\sqrt{\frac{\hbar\omega_i}{4\pi\epsilon_0}}\,\hat{a}(\boldsymbol{q}_i,\omega_i)\,e^{i(\boldsymbol{q}_i\cdot\boldsymbol{\rho}+k_{iz}z)}+\text{c.c}, \quad (7)$$

where $\hat{\boldsymbol{E}}_i(\boldsymbol{r},\omega_i)$ is the quantized operator corresponding to the classical amplitude $\boldsymbol{E}_i(\boldsymbol{r},\omega_i)$ defined in Eq. (1) and $\hat{a}(\boldsymbol{q}_i,\omega_i)$ is the annihilation operator for the mode specified by its arguments. Upon comparing Eqs. (1) and (7), it is clear that for $A_i(\boldsymbol{q}_i,\omega_i,0)$ to effectively mimic the vacuum fluctuations, we must have $2\langle A_i(\boldsymbol{q}'_i,\omega'_i,0)A_i^*(\boldsymbol{q}_i,\omega_i,0)\rangle = \frac{\hbar\sqrt{\omega_i\omega'_i}}{4\pi\epsilon_0}\langle\text{vac}|\hat{a}_i(\boldsymbol{q}'_i,\omega'_i)\hat{a}_i^\dagger(\boldsymbol{q}_i,\omega_i)|\text{vac}\rangle$, where $|\text{vac}\rangle$ is the quantum state of the vacuum [46]. Using the relation $\langle\text{vac}|\hat{a}_i(\boldsymbol{q}'_i,\omega'_i)\hat{a}_i^\dagger(\boldsymbol{q}_i,\omega_i)|\text{vac}\rangle = \delta(\boldsymbol{q}'_i-\boldsymbol{q}_i)\delta(\omega_i-\omega'_i)$ from quantum theory [48], we obtain

$$\langle A_i(\boldsymbol{q}'_i,\omega'_i,0)A_i^*(\boldsymbol{q}_i,\omega_i,0)\rangle = \frac{\hbar\omega_i}{8\pi\epsilon_0}\delta(\boldsymbol{q}_i-\boldsymbol{q}'_i)\delta(\omega_i-\omega'_i). \quad (8)$$

Thus, we find that the different modes of the classical "vacuum" are indeed completely uncorrelated, and the scaling factor $\hbar\omega_i/8\pi\epsilon_0$ ensures consistency with the zero-point energy of the quantum vacuum fluctuations. The above derivation of Eq. (8) is the only calculation in this paper that explicitly appeals to quantum theory [49].

We now substitute Eq. (8) into Eq. (6), replace the slowly-varying term ω_i by its central value ω_{i0}, and take it outside the integral to obtain

$$\langle A_s(\boldsymbol{q}_s,\omega_s,L)A_s^*(\boldsymbol{q}'_s,\omega'_s,L)\rangle$$
$$= \frac{\hbar\omega_{i0}d_{\text{eff}}^2 L^2\omega_s^2\omega_s'^2}{8\pi\epsilon_0 k_{sz}k'_{sz}c^4}$$
$$\times \iint d\omega_i d\boldsymbol{q}_i\langle A_p(\boldsymbol{q}_s+\boldsymbol{q}_i,\omega_s+\omega_i)A_p^*(\boldsymbol{q}'_s+\boldsymbol{q}_i,\omega'_s+\omega_i)\rangle$$
$$\times \text{sinc}(\Delta k_z L/2)\text{sinc}(\Delta k'_z L/2)\,e^{i(\Delta k_z-\Delta k'_z)L/2}. \quad (9)$$

The above expression is consistent with the reduced density matrix of the signal photon obtained from the full quantum-mechanical treatment of low-gain SPDC [6–8]. The integration over the classical "vacuum" modes on the right-hand side of Eq. (9) is formally equivalent to performing a partial trace of the two-photon density matrix over the idler photon. Thus, the generated field from DFG in the low-gain regime replicates the signal field from SPDC with respect to second-order spatiotemporal correlations, and in this context the classical "vacuum" field in DFG plays a role equivalent to that of the idler field from SPDC. However, we emphasize that the latter equivalence is valid *only* for the specific purpose of deriving the second-order correlations of the signal field because the correlations of the classical "vacuum" do *not* reflect those of the idler field in reality.

B. High-gain regime

When the pump power is high and consequently, the nonlinear interaction is strong, we can no longer ignore the longitudinal growth of the seeding classical "vacuum". As a

result, the derivation of the signal field correlations is slightly more involved and proceeds a bit differently. In particular, we will now use the position-time representation $V_p(\boldsymbol{\rho}, t)$ of the pump amplitude, which is related to the Fourier amplitude $A_p(\boldsymbol{q}_p, \omega_p)$ as

$$V_p(\boldsymbol{\rho}, t) = \iint d\boldsymbol{q}_p d\omega_p A_p(\boldsymbol{q}_p, \omega_p) e^{i(\boldsymbol{q}_p \cdot \boldsymbol{\rho} - \omega_p t)}. \qquad (10)$$

We invert the Fourier relation in Eq. (10), substitute it into Eq. (4), and differentiate with respect to z to obtain

$$\frac{\partial^2 A_s(\boldsymbol{q}_s, \omega_s, z)}{\partial z^2} = \frac{2id_{\text{eff}}\omega_s^2}{(2\pi)^3 k_{sz} c^2} \iiiint d\omega_i \, d\boldsymbol{q}_i \, d\boldsymbol{\rho} \, dt$$
$$\times V_p(\boldsymbol{\rho}, t) e^{-i(\boldsymbol{q}_p \cdot \boldsymbol{\rho} - \omega_p t)} e^{i\Delta k_z z} \left[\frac{\partial A_i^*(\boldsymbol{q}_i, \omega_i, z)}{\partial z} \right.$$
$$\left. + i\Delta k_z A_i^*(\boldsymbol{q}_i, \omega_i, z) \right]. \qquad (11)$$

In most experiments, the angular and frequency bandwidths $\delta\boldsymbol{q}_p$ and $\delta\omega_p$ of the pump are much smaller than the corresponding bandwidths $\delta\boldsymbol{q}_s$ and $\delta\omega_s$ of the generated SPDC field, respectively. Under this condition of a "narrow-band pump", the variation of Δk_z with respect to $\boldsymbol{q}_p$ and ω_p is much slower than that of $A_p(\boldsymbol{q}_p, \omega_p)$, which is usually sharply-peaked around the central wavevector $\boldsymbol{q}_{p0} = 0$ and the central pump frequency ω_{p0}. As a result, one can define $\Delta \bar{k}_z$ as the central value of Δk_z evaluated for the conditions $\boldsymbol{q}_s + \boldsymbol{q}_i = 0$ and $\omega_s + \omega_i = \omega_{p0}$, approximate $\Delta k_z \approx \Delta \bar{k}_z$ (this approximation is exactly true only for the monochromatic plane-wave pump case) in the second term on the right-hand side of the integral, and take it outside the integral. We note that any quantity appearing with an overbar notation in the rest of this paper must be understood as the central value of that quantity evaluated for the aforementioned conditions. Using Eqs. (4) and (10) in Eq. (11) (see Appendix B 1 for details), we obtain

$$\frac{\partial^2 A_s(\boldsymbol{q}_s, \omega_s, z)}{\partial z^2} - i\Delta \bar{k}_z \frac{\partial A_s(\boldsymbol{q}_s, \omega_s, z)}{\partial z}$$
$$- \bar{G}^2(\boldsymbol{\rho}, t) A_s(\boldsymbol{q}_s, \omega_s, z) = 0, \qquad (12)$$

where we have defined

$$G^2(\boldsymbol{\rho}, t) = \frac{4d_{\text{eff}}^2 \omega_s^2 \omega_i^2}{k_{sz} k_{iz} c^4} |V_p(\boldsymbol{\rho}, t)|^2. \qquad (13)$$

Upon solving Eq. (12) subject to the initial conditions $A_s(\boldsymbol{q}_s, \omega_s, z=0) = 0$ and $\partial A_s(\boldsymbol{q}_s, \omega_s, z)/\partial z|_{z=0}$ evaluated using Eqs. (4a) and (10), we obtain (see Appendix B 2 for details)

$$A_s(\boldsymbol{q}_s, \omega_s, L)$$
$$= \frac{2id_{\text{eff}}\omega_s^2}{(2\pi)^3 k_{sz} c^2} \iiiint d\omega_i \, d\boldsymbol{q}_i \, d\boldsymbol{\rho} \, dt \, V_p(\boldsymbol{\rho}, t)$$
$$\times e^{-i(\boldsymbol{q}_p \cdot \boldsymbol{\rho} - \omega_p t)} A_i^*(\boldsymbol{q}_i, \omega_i, 0) \left[\frac{\sinh \Gamma(\Delta \bar{k}_z, \boldsymbol{\rho}, t) L}{\Gamma(\Delta \bar{k}_z, \boldsymbol{\rho}, t)} \right]$$
$$\times e^{i(\Delta k_z - \Delta \bar{k}_z/2)L}, \qquad (14)$$

where

$$\Gamma(\Delta \bar{k}_z, \boldsymbol{\rho}, t) \equiv \sqrt{\bar{G}^2(\boldsymbol{\rho}, t) - \left(\frac{\Delta \bar{k}_z}{2} \right)^2}. \qquad (15)$$

Using Eqs. (8) and (14), and taking $\omega_i \approx \omega_{i0}$ outside the integral, we find (see Appendix B 3 for the detailed calculation)

$$\langle A_s(\boldsymbol{q}_s, \omega_s, L) A_s^*(\boldsymbol{q}_s', \omega_s', L) \rangle$$
$$= \frac{\hbar\omega_{i0} d_{\text{eff}}^2 \omega_s^2 \omega_s'^2}{(2\pi)^4 \epsilon_0 k_{sz} k_{sz}' c^4}$$
$$\times \iint d\boldsymbol{\rho} \, dt \, \langle |V_p(\boldsymbol{\rho}, t)|^2 \rangle \, e^{-i[(\boldsymbol{q}_s - \boldsymbol{q}_s')\boldsymbol{\rho} - (\omega_s - \omega_s')t]}$$
$$\times \left[\frac{\sinh \Gamma(\Delta \bar{k}_z, \boldsymbol{\rho}, t) L}{\Gamma(\Delta \bar{k}_z, \boldsymbol{\rho}, t)} \right] \left[\frac{\sinh \Gamma(\Delta \bar{k}_z', \boldsymbol{\rho}, t) L}{\Gamma(\Delta \bar{k}_z', \boldsymbol{\rho}, t)} \right]$$
$$\times e^{i(\Delta \bar{k}_z - \Delta \bar{k}_z')L/2}. \qquad (16)$$

The above expression quantifies the second-order spatiotemporal correlations of the generated field for a narrow-band pump in the high-gain regime. It may be verified that Eq. (16) is consistent with previous *quantum* derivations of the high-gain SPDC field correlations for a monochromatic plane-wave pump [5] (see also Ref. [50], where analogous expressions have been derived in the quantum treatment of Josephson traveling wave parametric amplifiers) and a narrow-band pump [16] (see Eq. B.1 in Appendix B of Ref. [51], where the expression derived in Ref. [16] has been used for quantifying spatial correlations in degenerate SPDC with a quasimonochromatic pump with narrow angular bandwidth). We however note that owing to the "narrow-band" approximation involved in the above derivation, in the low-gain limit $G(\boldsymbol{\rho}, t) \to 0$ wherein $\Gamma(\Delta \bar{k}_z, \boldsymbol{\rho}, t) \to i\Delta \bar{k}_z/2$, Eq. (16) is in general only *approximately* equivalent to Eq. (9). Nevertheless, it can be verified that the equivalence is exact for the case of a monochromatic plane-wave pump, for which the "narrow-band" approximation is exactly true. In the following section, we experimentally test the predictions of Eq. (16) by measuring the far-field intensity profile, OAM spectrum, and frequency spectrum in high-gain SPDC for increasing gain with a pulsed Gaussian pump.

III. SINGLE-CRYSTAL SETUP: EXPERIMENTS AND THEORY

In our experimental setup depicted in Fig. 2, a 355-nm Nd:YAG laser (EKSPLA PL2231) emits 30 ps long pulses of vertically-polarized light at a repetition rate of 50 Hz. These pulses are spatially-filtered and used to pump a 3-mm-long type-I β-barium borate (BBO) crystal (cut to produce horizontally-polarized collinear degenerate emission for perpendicular incidence of a vertically-polarized pump) placed at the pump's waist plane. A combination of a half-wave plate (HWP) and polarizing beamsplitter (PBS) is used to control the pump amplitude reaching the crystal. This pump amplitude is inferred up to an overall scaling factor from energy measurements using the energy meter (Coherent EnergyMax USB-J-10MB-HE). The beam-waist size w_p, defined as the $1/e^2$ half width of the intensity profile at the waist plane, was measured using a Gentec Beamage-3.0 beam profiler to be
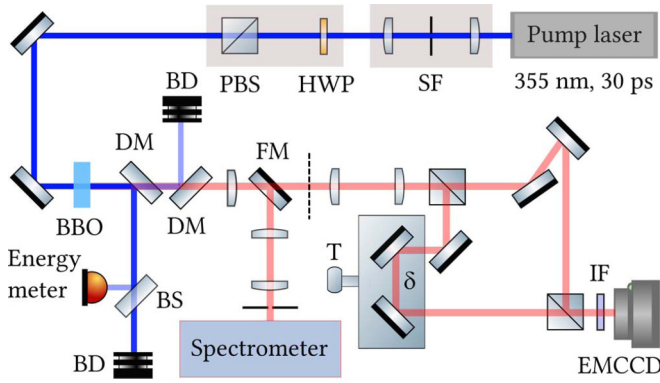
FIG. 2. Schematic of the experimental setup used for measuring the far-field intensity profile, OAM spectrum, and wavelength spectrum in high-gain SPDC for increasing pump strengths. SF: spatial filter, HWP + PBS: half-wave plate + polarizing beamsplitter combination for pump amplitude control, BBO: β-barium borate nonlinear crystal, DM: dichroic mirror, BD: beam dump, BS: beamsplitter, FM: flip mirror, T: translation stage to control the interferometric phase δ, IF: interference filter centered at 710 nm.

$w_p = 185 \, \mu$m. The residual pump after the crystal is removed by means of two dichroic mirrors (DMs), and the generated SPDC field is guided towards different parts of the setup for measurements as described in the following subsections.

A. Far-field intensity

We place a lens with its focal plane coinciding with the crystal output face, and directly image the SPDC far-field on an Andor Ixon-897 EMCCD camera (pixel size $16 \, \mu$m $\times$ $16 \, \mu$m) that is placed at the plane indicated by the dashed line after the flip mirror (FM) location depicted in Fig. 2. The crystal orientation was approximately set to satisfy the collinear emission, and a 10-nm interference filter (IF) centered at the degenerate wavelength $\lambda_s = 2\lambda_{p0} = 710$ nm was placed at the camera aperture. We rotate the HWP across different angles and acquire five sets of ten images each of the SPDC far-field for each corresponding pump amplitude, which is simultaneously measured using the energy meter. We then take diametric slices along the horizontal and vertical axes of each SPDC profile and compute the full widths at half maximum (FWHMs). We observe an asymmetry of about 4% between the widths in the two directions due to spatial walk-off. However, we ignore walk-off effects in our study and consider the mean of the two widths as the width of the far-field profile. The FWHM width is converted from number of pixels to angle in milliradians by using the camera pixel size and the focal length of the collimating lens.

For obtaining the theoretical prediction, we fix the variables in the temporal degree of freedom by assuming degenerate SPDC $\lambda_s = 710$ nm with a quasimonochromatic pump of wavelength $\lambda_{p0} = 355$ nm. We verify that the pump angular bandwidth $\delta \boldsymbol{q}_p = 2/w_p^2 \approx 58 \, \mathrm{mm}^{-2}$ is indeed much smaller than the SPDC angular bandwidth $\delta \boldsymbol{q}_s = |\boldsymbol{k}_s|/L \approx 4910 \, \mathrm{mm}^{-2}$ [16]. We then use Eq. (16) to compute the far-field

intensity as

$$
\langle |A_s(\boldsymbol{q}_s)|^2 \rangle = \frac{K_{\mathrm{arb}}}{k_{sz}^2} \int d\boldsymbol{\rho} \, \langle |V_p(\boldsymbol{\rho})|^2 \rangle
$$
$$
\times \left| \frac{\sinh \Gamma(\Delta \bar{k}_z, \boldsymbol{\rho}) L}{\Gamma(\Delta \bar{k}_z, \boldsymbol{\rho})} \right|^2, \tag{17}
$$

where K_{arb} is an overall scaling constant. Throughout this paper, the quantity K_{arb} must be interpreted as an arbitrary scaling factor whose value is irrelevant for our purposes. The frequency-time coordinates have been suppressed for brevity.

For our experiments, the pump field profile and phase-mismatch are given by

$$
V_p(\boldsymbol{\rho}) = g \exp\{-|\boldsymbol{\rho}|^2/w_p^2\}, \tag{18a}
$$
$$
\Delta \bar{k}_z = |\boldsymbol{k}_p| - 2\sqrt{|\boldsymbol{k}_s|^2 - |\boldsymbol{q}_s|^2}, \tag{18b}
$$

where g is a pump amplitude scaling factor, $|\boldsymbol{k}_s| = 2\pi n_{so}/\lambda_s$, $|\boldsymbol{k}_p| = 2\pi \eta_p(\theta_p)/\lambda_{p0}$, θ_p is the angle between the pump propagation direction and the optic axis inside the crystal, and $\eta_p(\theta_p) = n_{pe} n_{po}/\sqrt{n_{po}^2 \sin^2 \theta_p + n_{pe}^2 \cos^2 \theta_p}$ is the effective refractive index of the extraordinary-polarized pump inside the crystal [52]. The values $n_{p(e)o}$ and n_{so} of the (extra)ordinary and ordinary refractive indices of BBO for the pump and signal wavelengths, respectively, can be obtained using the Sellmeier relations [53]

$$
n_e^2(\lambda) = 2.7405 + \frac{0.0184}{\lambda^2 - 0.0179} - 0.0155\lambda^2, \tag{19a}
$$
$$
n_o^2(\lambda) = 2.3730 + \frac{0.0128}{\lambda^2 - 0.0156} - 0.0044\lambda^2, \tag{19b}
$$

where λ is the corresponding wavelength in microns. Using these parameters with Eq. (17), we perform a least-squares fit between theory and experiment of the logarithmic total far-field intensity with g as the fit parameter. The value of θ_p for the simulations is allowed to have a small offset from the collinear emission condition $\theta_p^{(\mathrm{coll})} = 32.914°$ because in experiments, θ_p is set by hand to approximately satisfy collinear emission. We ignore walk-off effects and exploit the rotational symmetry of the pump and the SPDC field to significantly speed up our simulations.

We depict our experimental and theoretical results in Fig. 3. In our simulations, we chose $\theta_p = 32.9105°$, which is less than $0.004°$ away from $\theta_p^{(\mathrm{coll})} = 32.914°$. The experimental and theoretical far-field intensity profiles for $g = 3.5$ (in arbitrary units) are shown in Figs. 3(a) and 3(b), respectively. Apart from some visible aberrations in the experimental image Fig. 3(a) that appear due to burnt spots and dust on a dichroic mirror, the profiles match closely. In Fig. 3(c), we show the trends of the full widths at half maximum (FWHMs) of diametric slices and total intensities of the far-field profiles with increasing pump amplitudes. The observed increasing trend of the FWHMs indicating the broadening of the angular spectrum with gain has also been reported previously [31]. Here, we find good agreement of our classical model's predictions with experimental observations.
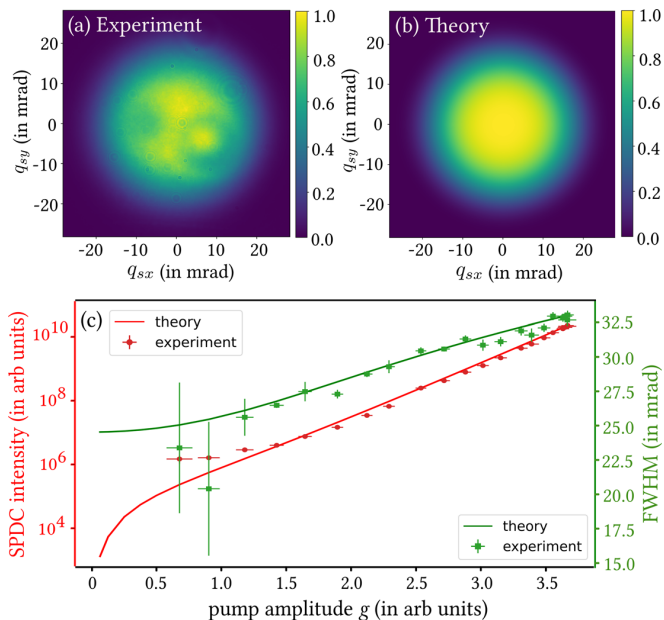
FIG. 3. Broadening of the far-field intensity profile of the SPDC field with increasing gain. (a) and (b) depict the experimental and theoretical images for $g = 3.5$. The experimental and theoretical total intensities and full widths at half maximum (FWHMs) of diametric slices of such profiles for increasing pump amplitudes are depicted in (c).

B. OAM spectrum

In SPDC with a zero-OAM Gaussian pump field, OAM conservation constrains the form of the generated state to a high-dimensional superposition involving signal and idler modes with opposite anticorrelated OAM values. In the low-gain regime, these modes are populated by one photon each [54], whereas in the high-gain regime, the same modes can be populated by higher but correlated numbers of photons [55]. In both cases, the second-order spatial correlations of the signal field are equivalent to those of a field that is an incoherent mixture of different OAM states, and the distribution of the weights of the OAM states is referred to as the OAM spectrum. We now study the behavior of the OAM spectrum in high-gain SPDC for increasing pump strengths.

We define the polar coordinates (q_s, ϕ_s) of $\boldsymbol{q}_s$ to be related to the Cartesian coordinates as $(q_s \sin \phi_s, q_s \cos \phi_s) = (q_{sx}, q_{sy})$. The generated field of Eq. (14) can be written as [56]

$$A_s(q_s, \phi_s) = \sum_{l=-\infty}^{+\infty} \sum_{p=0}^{\infty} \alpha_{lp} LG_p^l(q_s) e^{il\phi_s}, \quad (20)$$

where l and p are the azimuthal and radial indices of the Laguerre-Gauss mode functions $LG_p^l(q_s) e^{il\phi_s}$, and α_{lp} are stochastic coefficients that satisfy $\sum_p \langle \alpha_{lp} \alpha_{l'p}^* \rangle = S_l \delta_{ll'}$, where $\delta_{ll'}$ is the Kronecker delta symbol. The quantities S_l, which include contributions from all the constituent radial modes, are collectively referred to as the OAM spectrum. The angular coherence function $W(\phi_{s1}, \phi_{s2}) = W(\phi_{s1} - \phi_{s2})$ defined

as [56,57]

$$W(\phi_{s1} - \phi_{s2}) = \int dq_s \, q_s \, \langle A_s(q_s, \phi_{s1}) A_s^*(q_s, \phi_{s2}) \rangle, \quad (21)$$

has been shown to be related to the OAM spectrum S_l by the Fourier transform relation [56,57]

$$S_l = \int_{-\pi}^{\pi} d\Delta\phi \, W(\Delta\phi) \, e^{il\Delta\phi}. \quad (22)$$

Thus, the angular coherence function $W(\phi_s, -\phi_s) = W(2\phi_s)$ can be computed using Eqs. (16) and (21), following which Eq. (22) can be used to obtain the OAM spectrum.

In our experiments, we employ the interferometric technique reported in Ref. [56] to measure the OAM spectrum of the high-gain SPDC field. As shown in Fig. 2, the SPDC field is incident onto a Mach-Zehnder interferometer with an odd and even number of mirrors in the two arms, and its far-field interferograms are imaged using the EMCCD camera. The constructive and destructive interferograms are acquired by changing the interferometric phase δ using the translation stage, and their difference image is used to compute the OAM spectrum [56]. However, this direct procedure results in large errors in the value of S_0 due to shot-to-shot fluctuations in the pump energy. We partially address this problem by averaging the interferograms over two hundred pulses, but interferometric phase drifts prevent us from increasing the acquisition time further. Moreover, the larger acquisition times also introduce errors due to systematic energy drifts of the laser. Therefore, we normalize the constructive and destructive interferograms such that the intensities in a 20×20 pixels region away from the central interference fringe for both images are the same. Such a normalization effectively simulates the situation where the two interferograms were obtained for identical pump energies and almost entirely eliminates the fluctuation in S_0. In addition, the sum image of the two interferograms after this normalization effectively approximates the intensity profile of the SPDC field, which is then used for fitting the experimental results to the model's predictions. In this way, we obtain the OAM spectra and the total intensities for different pump amplitudes.

We compute the theoretical predictions using the same parameters that were used in the previous subsection. We perform a fit between theory and experiment of the logarithmic total intensities for different pump amplitudes with g as the fit parameter. Using Eqs. (16) and (21), we then compute $W(\phi_s, -\phi_s)$, and subsequently use Eq. (22) to compute the OAM spectrum for each pump amplitude. For our simulations, we choose $\theta_p = 32.894°$, which is only $0.02°$ away from $\theta_p^{(\text{coll})} = 32.914°$. A slight discrepancy between the values of θ_p in this subsection and the previous subsection is expected because the crystal was realigned between the two rounds of experiments. The rotational and reflection symmetries of the pump and SPDC fields can be used to significantly speed up the computations.

We depict our experimental and theoretical results in Fig. 4. The constructive and destructive experimentally-measured interferograms for $g = 3.0$ (in arb units) are depicted in Figs. 4(a) and 4(b). The measured OAM spectrum with the theoretically-predicted spectrum are shown in Fig. 4(c). The width of the OAM spectrum can be quantified using the
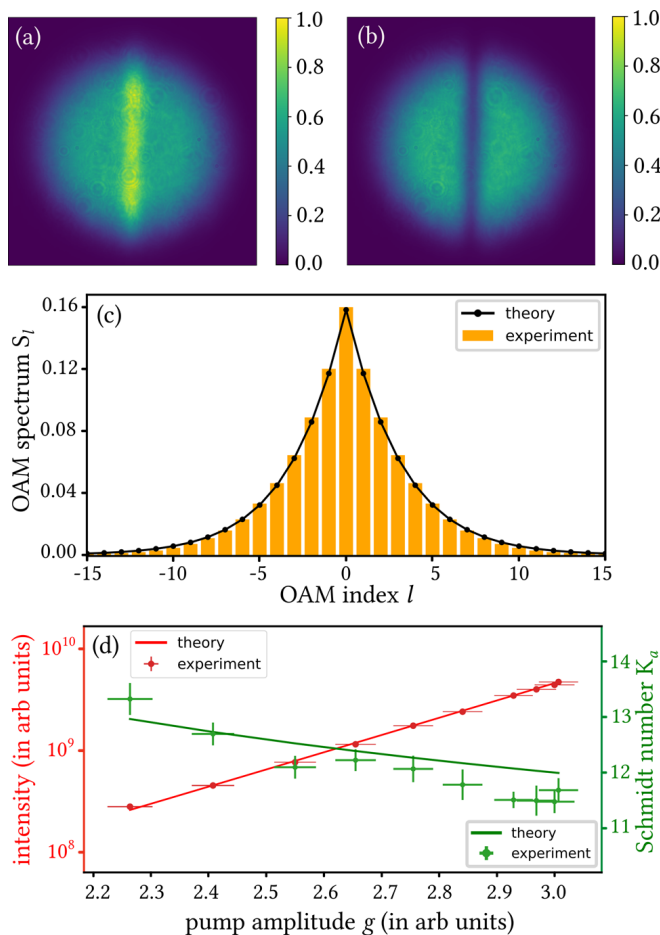
FIG. 4. Narrowing of the OAM spectrum of the SPDC signal field with increasing gain. (a) and (b) are the constructive and destructive interferograms, and (c) depicts the measured OAM spectrum along with the theoretical prediction for $g = 3.0$. (d) depicts the total intensity and Schmidt number $K_a \equiv 1/\sum_l S_l^2$ as a function of pump amplitude g.

angular Schmidt number $K_a \equiv 1/\sum_l S_l^2$, where the spectrum is normalized such that $\sum_l S_l = 1$. In Fig. 4(d), we depict the trends of the total intensity and the Schmidt number for increasing pump amplitudes. The decreasing Schmidt number implies that the OAM spectrum narrows with increasing gain. Again, we find that our experimental measurements are in good agreement with the predictions of our classical model.

C. Wavelength spectrum

We raise the flip mirror depicted in Fig. 2 and guide the SPDC field into a spectrometer to measure its wavelength spectrum. The spectrometer is an imaging spectrograph (Princeton Instruments Acton Series SP2558 500 mm triple-grating) with a CCD camera (PIXIS:100BR eXcelon, pixel size 20 μm $\times$ 20 μm). An aperture of 1-mm radius is used to select only the central portion of the collinear emission far-field corresponding to $\boldsymbol{q}_s \approx 0$, and a lens with focal length 500 mm is used to focus the light from the aperture onto the entrance slit of the spectrometer. We record each CCD image with an acquisition time of 4000 ms, and integrate the

photoelectron counts over the vertical axis of the image to obtain the spectrum. We record ten spectra for each pump amplitude over the range from 610 nm to 810 nm, and to cover this range, we repeat the acquisition for different angular positions of the grating (1200 grooves per mm, 750 nm blaze). We apply a median filter to the recorded spectra to eliminate outlier peaks that appear at random locations.

For evaluating the theoretically predicted spectrum, we set $\boldsymbol{q}_s = 0$ in collinear SPDC, and obtain the frequency spectrum from Eq. (16) as

$$\langle |A_s(\omega_s)|^2 \rangle = K_{\mathrm{arb}}\, \omega_s^2 \iint d\boldsymbol{\rho}\, dt\, \langle |V_p(\boldsymbol{\rho}, t)|^2 \rangle$$

$$\times \left| \frac{\sinh \Gamma(\Delta \bar{k}_z, \boldsymbol{\rho}, t)L}{\Gamma(\Delta \bar{k}_z, \boldsymbol{\rho}, t)} \right|^2. \qquad (23)$$

The spatial coordinates of the signal field have been suppressed for brevity. The wavelength spectrum $S(\lambda_s)$ can be computed using the relation $S(\lambda_s) = \langle |A_s(\omega_s)|^2 \rangle |d\omega_s/d\lambda_s|$ that upon using $\omega_s = 2\pi c/\lambda_s$ yields

$$S(\lambda_s) = K_{\mathrm{arb}} \langle |A_s(2\pi c/\lambda_s)|^2 \rangle / \lambda_s^2. \qquad (24)$$

We now compute $S(\lambda_s)$ using the relations,

$$V_p(\boldsymbol{\rho}, t) = g \exp\left\{ -\frac{t^2}{(2\Delta t)^2} \right\} \exp\left\{ -\frac{|\boldsymbol{\rho}|^2}{w_p^2} \right\}, \qquad (25a)$$
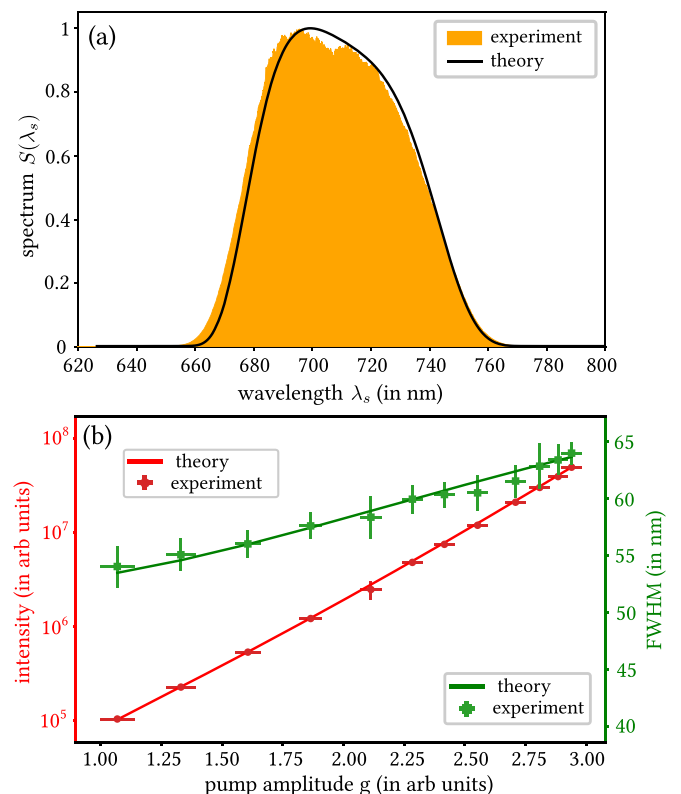

FIG. 5. Broadening of the wavelength spectrum of the SPDC signal field with increasing gain. (a) depicts the wavelength spectrum for $g = 2.8$. (b) depicts the total intensity and FWHM widths of the spectra for different pump amplitudes.
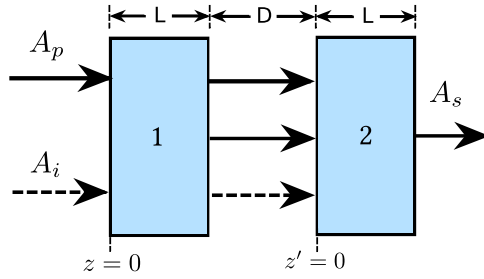
FIG. 6. Conceptual schematic depiction of SU(1,1) interference as interpreted in our classical model.

$$\Delta \bar{k}_z = \frac{2\pi \eta_p(\theta_p)}{\lambda_{p0}} - \frac{2\pi n_o(\lambda_s)}{\lambda_s} - \frac{2\pi n_o(\bar{\lambda}_i)}{\bar{\lambda}_i}, \quad (25b)$$

where g is a pump amplitude scaling factor, $\bar{\lambda}_i = 1/(1/\lambda_{p0} - 1/\lambda_s)$, and $\Delta t = 30/2.355 = 12.738$ ps, where we have converted the FWHM pulse width of the power to the standard deviation width [58]. Using these parameters and the dispersion relations (19), we perform a least-squares fit of the total intensities of the recorded spectra to the total intensities predicted by Eq. (23) with g as the fit parameter. We then use the fit value of g to compute the theoretically-predicted spectra for different pump amplitudes. The spatial rotational symmetry of the pump can be exploited to significantly reduce computation time.

In Fig. 5, we depict our experimental and theoretical results. In Fig. 5(a), we depict the experimental and theoretical wavelength spectrum for $g = 2.8$ (in arb units), and in Fig. 5(b), we depict the total intensities and the FWHM widths of the spectra for different pump strengths. The increasing FWHM width implies that the wavelength spectrum gets broader with increasing pump strength in high-gain SPDC [30]. Our experimental results are in good agreement with the theoretical predictions of our classical model.

IV. TWO-CRYSTAL SETUPS: THEORY

A. SU(1,1) interference

SU(1,1) interferometers are nonlinear interferometers that can be created by essentially replacing the beamsplitters in linear SU(2) interferometers, such as Mach-Zehnder interferometers, by nonlinear crystals [41,42,59]. It is known that such interferometers can achieve a phase sensitivity approaching the Heisenberg limit with the important advantage that they have a better loss tolerance than linear SU(2) interferometers employing squeezed states of light. In addition to phase metrology [60], SU(1,1) interferometers are also useful for applications such as radiation shaping [61], microscopy [62], optical coherence tomography [63], and sensing [64].

We consider the SU(1,1) setup shown in Fig. 6 that involves two crystals 1 and 2, each of length L, separated by an air gap of length D. We define the longitudinal coordinate z' such that $z' = 0$ corresponds to the input face of crystal 2. We assume that D is small enough such that the second crystal is in the near field of the first crystal. Thus, the generated fields from the two crystals can be assumed to overlap perfectly. As the field A_j for $j = p, s, i$ propagates across crystal 1 and the air

gap to reach crystal 2, it acquires a phase $k_{jz}L + k_{jz}^{(\text{air})}D$, where $k_{jz}^{(\text{air})}$ represents the longitudinal wavevector component of the corresponding field in air. As a result, the field generated in crystal 2 follows the relation

$$\frac{\partial A_s(\boldsymbol{q}_s, \omega_s, z')}{\partial z'} = \frac{2id_{\text{eff}}\omega_s^2}{k_{sz}c^2} \iint d\omega_i \, d\boldsymbol{q}_i \, A_p(\boldsymbol{q}_p, \omega_p)$$
$$\times e^{i[\Delta k_z L + \Delta k_z^{(\text{air})}D]} A_i^*(\boldsymbol{q}_i, \omega_i, z') e^{i\Delta k_z z'}, \quad (26)$$

where $\Delta k_z^{(\text{air})} = k_{pz}^{(\text{air})} - k_{sz}^{(\text{air})} - k_{iz}^{(\text{air})}$ is the longitudinal phase-mismatch in air. Using Eqs. (4a) and (26), the net field $A_s(\boldsymbol{q}_s, \omega_s)$ at the output of the interferometer can be written as

$$A_s(\boldsymbol{q}_s, \omega_s) = \frac{2id_{\text{eff}}\omega_s^2}{k_{sz}c^2} \iint d\omega_i \, d\boldsymbol{q}_i \, A_p(\boldsymbol{q}_p, \omega_p)$$
$$\times \left[\int_0^L dz \, A_i^*(\boldsymbol{q}_i, \omega_i, z) e^{i\Delta k_z z} + e^{i[\Delta k_z L + \Delta k_z^{(\text{air})}D]} \right.$$
$$\times \left. \int_0^L dz' \, A_i^*(\boldsymbol{q}_i, \omega_i, z') e^{i\Delta k_z z'} \right]. \quad (27)$$

In what follows, we derive the second-order spatiotemporal correlations of the output field in low- and high-gain regimes, and illustrate the interference in the spatial domain through numerical simulations.

1. Low-gain regime

In the low-gain regime, as the interaction is weak, the longitudinal growth of the classical "vacuum" across both the crystals is negligible. Therefore, we approximate $A_i^*(\boldsymbol{q}_i, \omega_i, z) \approx A_i^*(\boldsymbol{q}_i, \omega_i, 0)$ in both terms of the right-hand side of Eq. (27), and perform the integrations over z and z' to obtain

$$A_s(\boldsymbol{q}_s, \omega_s) = \frac{d_{\text{eff}}L\omega_s^2}{k_{sz}c^2} \iint d\omega_i \, d\boldsymbol{q}_i \, A_p(\boldsymbol{q}_p, \omega_p) A_i^*(\boldsymbol{q}_i, \omega_i, 0)$$
$$\times \text{sinc}(\Delta k_z L/2) \, e^{i\Delta k_z L/2}$$
$$\times \left\{ 1 + e^{i[\Delta k_z L + \Delta k_z^{(\text{air})}D]} \right\}. \quad (28)$$

Using the above equation along with Eq. (8), we obtain

$$\langle A_s(\boldsymbol{q}_s, \omega_s) A_s^*(\boldsymbol{q}_s', \omega_s') \rangle$$
$$= \frac{\hbar \omega_{i0} d_{\text{eff}}^2 L^2 \omega_s^2 \omega_s'^2}{8\pi \epsilon_0 k_{sz} k_{sz}' c^4} \iint d\omega_i \, d\boldsymbol{q}_i$$
$$\times \langle A_p(\boldsymbol{q}_s + \boldsymbol{q}_i, \omega_s + \omega_i) A_p^*(\boldsymbol{q}_s' + \boldsymbol{q}_i, \omega_s' + \omega_i) \rangle$$
$$\times \text{sinc}(\Delta k_z L/2) \text{sinc}(\Delta k_z' L/2) \, e^{i(\Delta k_z - \Delta k_z')L/2}$$
$$\times \{1 + e^{i[\Delta k_z L + \Delta k_z^{(\text{air})}D]}\} \{1 + e^{-i[\Delta k_z' L + \Delta k_z'^{(\text{air})}D]}\}. \quad (29)$$

The above expression quantifies the second-order spatiotemporal correlations of the output field of the SU(1,1) interferometer in the low-gain regime.

2. High-gain regime

In the high-gain regime, the initial classical "vacuum" $A_i^*(\boldsymbol{q}_i, \omega_i, 0)$ will first be amplified over the length L of crystal 1 to $A_i^*(\boldsymbol{q}_i, \omega_i, L)$, which then seeds the DFG process in

crystal 2. In order to quantify the growth of the classical "vacuum", we define $A_i^*(\boldsymbol{q}_i, \omega_i, z) = f(z) A_i^*(\boldsymbol{q}_i, \omega_i, 0)$, differentiate Eq. (4b) with respect to z, and make the "narrow-band pump" approximation to obtain

$$\frac{\partial^2 f(z)}{\partial z^2} + i \Delta \bar{k}_z \frac{\partial f(z)}{\partial z} - \bar{G}^2(\boldsymbol{\rho}, t) f(z) = 0. \qquad (30)$$

Solving the above Eq. (30) subject to the initial conditions $f(z = 0) = 1$ and $\partial f(z)/\partial z|_{z=0} = 0$, we obtain

$$f(z) = e^{-i\Delta\bar{k}_z z/2} \left\{ \cosh \Gamma(\Delta\bar{k}_z, \boldsymbol{\rho}, t)z \right.$$
$$\left. + \frac{i\Delta\bar{k}_z}{2\Gamma(\Delta\bar{k}_z, \boldsymbol{\rho}, t)} \sinh \Gamma(\Delta\bar{k}_z, \boldsymbol{\rho}, t)z \right\}. \qquad (31)$$

The above relation quantifies the growth of the classical "vacuum" inside crystal 1.

We now note that the generated field in crystal 2 will be governed by Eq. (12). Moreover, the field $A_s(\boldsymbol{q}_s, \omega_s, z' = 0)$ at the entrance of crystal 2 is given by Eq. (14) as the field remains constant through the air gap. In addition, $\partial A_s(\boldsymbol{q}_s, \omega_s, z')/\partial z'|_{z'=0}$ can be evaluated using Eq. (26). Solving Eq. (12) for the above initial conditions, we obtain (see Appendix B 4 for details)

$$A_s(\boldsymbol{q}_s, \omega_s) = \frac{4i d_{\text{eff}} \omega_s^2}{(2\pi)^3 k_{sz} c^2} \iiint d\omega_i \, d\boldsymbol{q}_i \, d\boldsymbol{\rho} \, dt \, V_p(\boldsymbol{\rho}, t)$$
$$\times \, e^{-i(\boldsymbol{q}_p \cdot \boldsymbol{\rho} - \omega_p t)} A_i^*(\boldsymbol{q}_i, \omega_i, 0) \left[\frac{\sinh \Gamma(\Delta\bar{k}_z, \boldsymbol{\rho}, t)L}{\Gamma(\Delta\bar{k}_z, \boldsymbol{\rho}, t)} \right]$$
$$\times \, e^{i(\Delta k_z - \Delta\bar{k}_z/2)L} h\big(\Delta k_z^{(\text{air})}, D\big), \qquad (32)$$

where we have defined

$$h\big(\Delta k_z^{(\text{air})}, D\big)$$
$$\equiv e^{i\Delta k_z^{(\text{air})}D/2} \left[\cosh \Gamma(\Delta\bar{k}_z, \boldsymbol{\rho}, t)L \cos\left\{ \Delta k_z^{(\text{air})}D/2 \right\} \right.$$
$$- \frac{\Delta\bar{k}_z}{2\Gamma(\Delta\bar{k}_z, \boldsymbol{\rho}, t)} \sinh \Gamma(\Delta\bar{k}_z, \boldsymbol{\rho}, t)L$$
$$\left. \times \sin\left\{ \Delta k_z^{(\text{air})}D/2 \right\} \right]. \qquad (33)$$

Using the above relations and Eq. (8), we obtain

$$\langle A_s(\boldsymbol{q}_s, \omega_s) A_s^*(\boldsymbol{q}_s', \omega_s') \rangle$$
$$= \frac{2\hbar\omega_{i0} d_{\text{eff}}^2 \omega_s^2 \omega_s'^2}{(2\pi)^4 \epsilon_0 k_{sz} k_{sz}' c^4} \iint d\boldsymbol{\rho} \, dt$$
$$\times \langle |V_p(\boldsymbol{\rho}, t)|^2 \rangle \, e^{-i[(\boldsymbol{q}_s - \boldsymbol{q}_s')\boldsymbol{\rho} - (\omega_s - \omega_s')t]}$$
$$\times \left[\frac{\sinh \Gamma(\Delta\bar{k}_z, \boldsymbol{\rho}, t)L}{\Gamma(\Delta\bar{k}_z, \boldsymbol{\rho}, t)} \right] \left[\frac{\sinh \Gamma(\Delta\bar{k}_z', \boldsymbol{\rho}, t)L}{\Gamma(\Delta\bar{k}_z', \boldsymbol{\rho}, t)} \right]$$
$$\times \bar{h}\big(\Delta k_z^{(\text{air})}, D\big) \bar{h}^*\big(\Delta k_z'^{(\text{air})}, D\big) \, e^{i(\Delta\bar{k}_z - \Delta\bar{k}_z')L/2}. \qquad (34)$$

The above equation quantifies the second-order spatiotemporal correlations of the output field of the SU(1,1) interferometer in the high-gain regime.
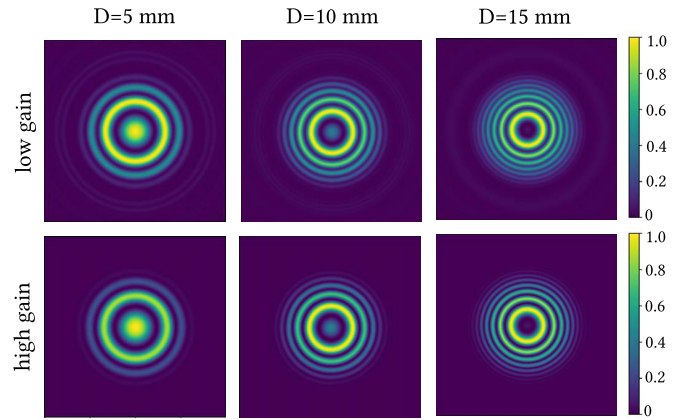

FIG. 7. SU(1,1) far-field interference patterns in the low- and high-gain regimes for increasing air gap lengths.

3. Numerical simulations in the spatial domain

We fix the frequency variables by restricting our attention to degenerate SPDC with a monochromatic pump, and suppress those variables for brevity. This restriction physically corresponds to placing a narrow-band filter centered at the degenerate emission wavelength after the second crystal. We numerically simulate collinear degenerate SPDC for the same parameters used in Sec. III A. For computing the phase mismatch Δk_z^{air}, we use the dispersion relation for air from Ref. [65], according to which the refractive index of air for the pump wavelength 355 nm is $n_p^{\text{air}} = 1.00028571$, and that for the signal (idler) wavelength 710 nm is $n_{s(i)}^{\text{air}} = 1.00027571$. We use Eq. (29) and $\Delta k_z = |\boldsymbol{q}_s - \boldsymbol{q}_i|^2/4k_s$ to compute the low-gain interference patterns, and use Eq. (34) to compute the high-gain interference patterns for different air gap lengths and depict them in Fig. 7. It is evident that in both gain regimes, the interference exhibits high visibility. In comparison to the low-gain patterns, the high-gain patterns have narrower extent and suppressed side-lobes. Moreover, with increasing air gap, the fringe separation reduces, and owing to the finite dispersion of air, the intensity at the center also varies. These predictions agree with previous experimental observations [31,66].

B. Induced coherence

In their seminal 1991 experiment [11], Zou, Wang, and Mandel built a modified SU(1,1) interferometric setup in which the signal fields from the two crystals were separated and superposed on a beamsplitter. Ordinarily, the signal fields from two distinct SPDC processes do not interfere with each other. However, Zou et al. [11] observed that when the idler paths from the two processes are aligned, the signal fields become mutually coherent and exhibit interference. This intriguing effect known as "induced coherence" has not only revealed fundamental insights about interference and indistinguishability [11,67], but has also been harnessed in a variety of applications such as imaging [43] and spectroscopy [68].

The physical origin of induced coherence has been extensively debated over the years since its inception [11,67,69–72]. In particular, the possibility of the coherence

originating from "induced emission", i.e., the idler photons from the first crystal stimulating emission in the second crystal, was recognized [11,67]. Zou *et al.* ruled out this possibility by performing their experiment at weak pump power where induced emission could be shown to be negligible. They argued that the induced coherence is a consequence of the signal photon paths being rendered indistinguishable by the alignment of the idler paths. Their theoretical analysis also supported this quantum interpretation by correctly predicting the experimentally-observed linear scaling of the interference visibility with respect to the transmittance of an object placed in the idler path between the crystals. Subsequently, Wiseman and Mølmer [70] performed a four-mode quantum calculation for arbitrary pump strengths and showed that the linear scaling of the visibility is the true signature of induced emission being negligible, and that the scaling is *not* linear when induced emission is significant. Moreover, they termed the former regime as "quantum", and the latter regime as "classical". Thus, it was implied that induced coherence without induced emission is an intrinsically quantum-mechanical effect with no classical explanation.

In more recent years, with the series of intriguing experimental demonstrations of "quantum imaging with undetected photons" [43], "quantifying the momentum correlation between two light beams by detecting one" [73], and "interference fringes controlled by noninterfering photons" [74], the question of whether induced coherence admits a classical explanation has gained renewed interest. While imaging with undetected light has been demonstrated in classical settings where an auxiliary external field stimulates the emission in both crystals [75,76], it was explicitly stated that the case of spontaneous low-gain emission cannot be explained within classical physics [76]. Subsequently, a theoretical study showed that induced coherence persists even when the pump field is a single photon Fock state, where the occurrence of stimulated emission is strictly impossible [72]. Based on this result, the authors concluded that any classical or semiclassical *explanation* of induced coherence is effectively ruled out. Nevertheless, we submit that their study does not preclude the existence of a classical *model* that successfully captures the various induced coherence-related experiments that have been performed so far in which the pump can be treated classically. In what follows, we show that the classical SPDC model of the present paper captures several important experimentally observed features of induced coherence in low- and high-gain regimes, including the linear scaling of the visibility for low gain that is often regarded as the signature quantum feature of induced coherence. We emphasize that our classical model does not constitute a complete classical *explanation*, and therefore, our results do not contradict Ref. [72] in any manner.

In Fig. 8, we depict the conceptual schematic of a prototypical induced coherence experiment involving two identical crystals as interpreted in the classical SPDC model of the present paper. The pump field is split into two equal parts: one part pumps crystal 1; the other part acquires a uniform phase ϕ_0 and pumps crystal 2. A classical "vacuum" field A_i seeds the process in crystal 1 and then encounters the object O that is assumed to have a complex field transmittance $T e^{i\gamma}$. The object O is modeled as a beamsplitter of splitting
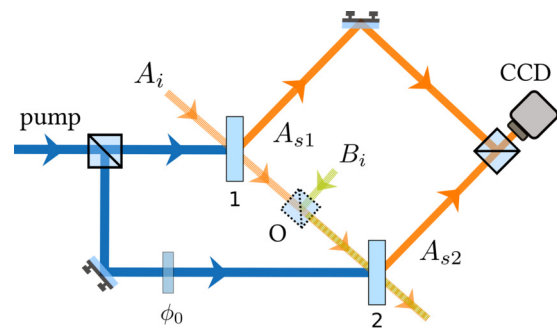

FIG. 8. Conceptual schematic of the induced coherence experiment [11] interpreted in classical SPDC. Here, the partially-transmissive object O is modeled as a beamsplitter.

ratio $T : \sqrt{1 - T^2}$ with a second classical "vacuum" B_i that is completely uncorrelated with the first classical "vacuum" A_i entering its other port. The output superposition of the two "vacua" from this hypothetical beamsplitter then seeds the process in crystal 2. The fields A_{s1} and A_{s2} generated from the two crystals 1 and 2 are superposed on a perfectly symmetric 50:50 beamsplitter and the interference is recorded on a CCD camera. We emphasize that Fig. 8 must be viewed as a conceptual depiction because the actual geometry of the setup can be entirely different. For instance, the experiment can also be implemented using collinear phase matching [43], but the underlying concept remains the same. In what follows, we fix the temporal variables by assuming degenerate SPDC with a quasimonochromatic pump, and derive the output spatial interference patterns recorded in the induced coherence experiment in low- and high-gain regimes.

1. Low-gain regime

In the low-gain regime, the growth of the "vacuum" $A_i^*(\mathbf{q}_i, 0)$ can be neglected. Using Eq. (5), the generated fields from the two crystals can then be written as

$$A_{s1}(\mathbf{q}_s) = \frac{K_{\text{arb}}}{k_{sz}} \int d\mathbf{q}_i \, A_p(\mathbf{q}_p) A_i^*(\mathbf{q}_i, 0) \, \text{sinc}(\Delta k_z L/2)$$
$$\times e^{i\Delta k_z L/2}, \tag{35a}$$

$$A_{s2}(\mathbf{q}_s) = \frac{K_{\text{arb}}}{k_{sz}} \int d\mathbf{q}_i \, A_p(\mathbf{q}_p) \, e^{i\phi_0} \, \text{sinc}(\Delta k_z L/2)$$
$$\times e^{i\Delta k_z L/2}[T \, e^{i\gamma} A_i^*(\mathbf{q}_i, 0) + \sqrt{1 - T^2} \, B_i^*(\mathbf{q}_i, 0)], \tag{35b}$$

The above fields overlap at the beamsplitter to yield the field $A_s(\mathbf{q}_s) = \{A_{s1}(\mathbf{q}_s) + A_{s2}(\mathbf{q}_s)\}/\sqrt{2}$ at the CCD camera. We now note that B_i has the same autocorrelations as that of A_i, i.e., $\langle B_i(\mathbf{q}_i', 0) B_i^*(\mathbf{q}_i, 0) \rangle = \langle A_i(\mathbf{q}_i', 0) A_i^*(\mathbf{q}_i, 0) \rangle = C\delta(\mathbf{q}_i - \mathbf{q}_i')$, where C is a scaling factor. However, B_i has no mutual correlations with A_i, i.e., $\langle A_i(\mathbf{q}_i', 0) B_i^*(\mathbf{q}_i, 0) \rangle = 0$. Using these relations, the measured intensity takes the form

$$I = \langle |A_s(\mathbf{q}_s)|^2 \rangle = \frac{K_{\text{arb}}}{k_{sz}^2} \int d\mathbf{q}_i |A_p(\mathbf{q}_p)|^2 \, \text{sinc}^2(\Delta k_z L/2)$$
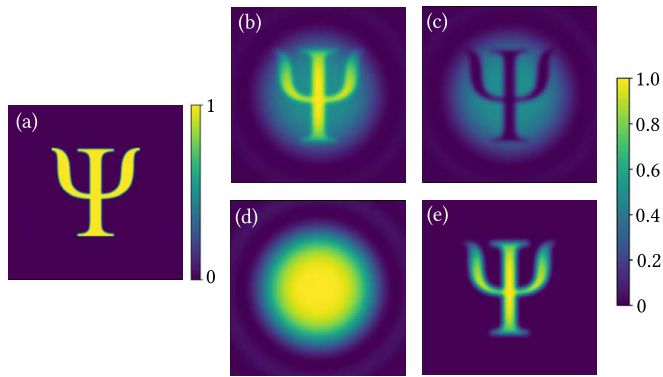$$\times \{1 + T \cos(\gamma + \phi_0)\}, \tag{36}$$

FIG. 9. Numerical simulations of a case similar to the one studied by Lemos *et al.* [43], where the object O has a binary structured transmission profile T. As shown in (a), we assume $T(\boldsymbol{q}_i)$ shaped in the Greek symbol Ψ. (b) and (c) are interferograms obtained for $\phi_0 = 0$ and $\phi_0 = \pi$, respectively. (d) and (e) are the sum and difference images, respectively.

In general, the transmittance T and phase γ could be spatially-structured, in which case they would explicitly depend on $\boldsymbol{q}_i$. However, when T and γ are uniform, the visibility $V(\boldsymbol{q}_s) = (I_{\max} - I_{\min})/(I_{\max} + I_{\min})$ scales linearly with T, in agreement with the quantum-mechanical prediction and experimental observations [11,67]. Thus, our classical model is able to correctly predict the linear scaling of the visibility with object transmittance in the low-gain regime—a feature that is often regarded as the quintessential signature of nonclassicality. We will now theoretically analyze two special cases of the object O within our classical model.

We first consider the case where the object O has a binary structured transmission profile $T(\boldsymbol{q}_i)$ and constant phase $\gamma = 0$ similar to the one studied by Lemos *et al.* [43]. Specifically, as shown in Fig. 9(a), we assume that $T(\boldsymbol{q}_i)$ has the shape of the Greek symbol Ψ. We assume collinear degenerate SPDC with the same parameters as chosen in Sec. III A. Using Eq. (36), we numerically compute the interferograms for $\phi_0 = 0$ and $\phi_0 = \pi$ and depict them in Figs. 9(b) and 9(c), respectively. The sum and difference images of these interferograms are depicted in Figs. 9(d) and 9(e), respectively. We note that the interferograms in Figs. 9(b) and 9(c) display the object O even though the interfering signal fields themselves have not directly interacted with the object, whereas the classical "vacuum" that has directly interacted with the object is never detected. This intriguing phenomenon was termed "quantum imaging with undetected photons" in Lemos *et al.* [43], and was explained in terms of the quantum-mechanical interpretation of induced coherence. Here, it is evident that the same feature is also captured within our classical model. We emphasize that while other studies have previously demonstrated this feature in classical settings involving a real external stimulating field [75,76], to our knowledge, this is the classical treatment applied to the spontaneous low-gain limit in which Zou *et al.* [11,67] and Lemos *et al.* [43] performed their experiments.

Next, we consider the case studied by Hochrainer *et al.* [73] in which the object O is a lens—a pure phase object with $T = 1$ and $\gamma = \lambda_i d \, |\boldsymbol{q}_i|^2/(4\pi)$ as depicted in Fig. 10(a). We set the
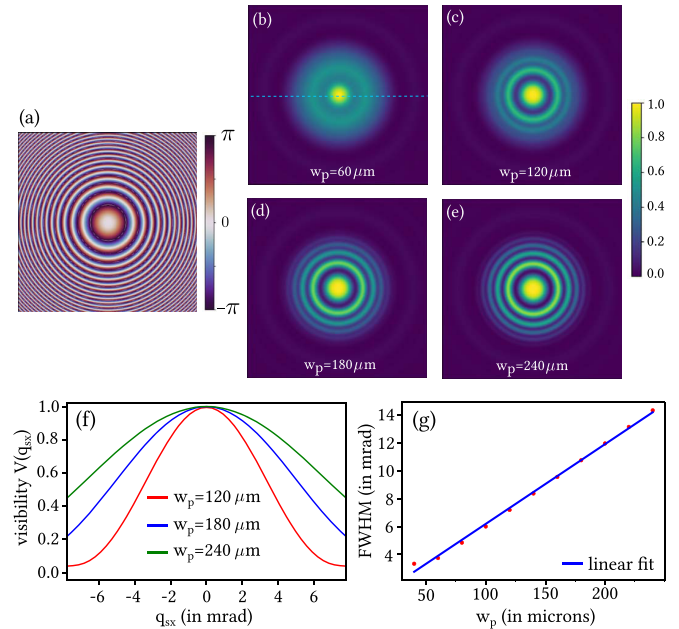

FIG. 10. Numerical low-gain simulations of the case considered in A. Hochrainer *et al.* [73], where object O is a lens with $T = 1$. (a) depicts the phase $\gamma \sim |\boldsymbol{q}_i|^2$ modulo 2π. [(b)–(e)] Depict interference patterns for increasing pump beam-waist w_p. (f) Depicts the visibility $V(q_{sx})$ computed along a horizontal slice, as shown in (b), through the center of the interferograms by varying the phase ϕ_0 from 0 to 2π, and (g) depicts the scaling of the FWHM of the visibility profiles with w_p.

equivalent free-space propagation distance $d = 22.6$ mm in our analysis, and study the interference for different values of the pump beam-waist w_p. The other parameters are chosen to be the same as those used in Sec. III A. In Fig. 10, we depict our numerical simulations of Eq. (36) corresponding to the low-gain regime. As shown in (b)–(e) for small values of w_p, the interference is blurred out away from the center, whereas for large values of w_p, the interference exhibits sharp contrast even for large radial distances. This effect can be interpreted in our classical model as follows: For small w_p, the pump has a large angular bandwidth, implying a large spread in $\boldsymbol{q}_p$. Consequently, the far-field intensity at $\boldsymbol{q}_s$ is a superposition of a large number of interference patterns corresponding to several different $\boldsymbol{q}_i$ that satisfy $\boldsymbol{q}_i = \boldsymbol{q}_p - \boldsymbol{q}_s$. As a result, the interference pattern is blurred. On the other hand, for large w_p, the pump's angular bandwidth is small, and consequently, the averaging effect is less pronounced leading to high interference visibility. For different values of w_p, we then compute the visibility $V(\boldsymbol{q}_s)$ along a horizontal slice, as shown in Fig. 10(b), through the center by numerically varying the phase ϕ_0 from 0 to 2π. As shown in Fig. 10(f), for small w_p, the visibility decays rapidly in the radial directions, whereas the decay is slower for larger w_p. In Fig. 10(f), we plot the FWHM of the visibility curves for increasing w_p along with a linear fit. This implies that the interference visibility can be used to infer the pump's angular bandwidth which, in the usual quantum-mechanical picture of SPDC, also determines the transverse momentum correlations between the signal and idler photons. Therefore, the

visibility can be used for "quantifying the momentum correlations between two photons by detecting one", as experimentally demonstrated by Hochrainer *et al.* [73]. Here, we find that our above results qualitatively agree with those depicted in Fig. 2 of Ref. [73], but the interpretation is classical within our model.

2. High-gain regime

In the high-gain regime, the initial "vacuum" $A_i^*(\boldsymbol{q}_i, 0)$ is amplified in crystal 1 to $A_i^*(\boldsymbol{q}_i, L) = A_i^*(\boldsymbol{q}_i, 0) f(L)$, which then superposes with the "vacuum" $B_i^*(\boldsymbol{q}_i, 0)$ from the other port of O to seed crystal 2. Using Eqs. (14) and (31), the fields from the two crystals can be written as

$$A_{s1}(\boldsymbol{q}_s) = \frac{K_{\mathrm{arb}}}{k_{sz}} \iint d\boldsymbol{q}_i \, d\boldsymbol{\rho} \, V_p(\boldsymbol{\rho}) e^{-i\boldsymbol{q}_p \cdot \boldsymbol{\rho}} \, e^{i(\Delta k_z - \Delta \bar{k}_z/2)L}$$
$$\times A_i^*(\boldsymbol{q}_i, 0) \left[\frac{\sinh \Gamma(\Delta \bar{k}_z, \boldsymbol{\rho})L}{\Gamma(\Delta \bar{k}_z, \boldsymbol{\rho})} \right], \quad (37a)$$

$$A_{s2}(\boldsymbol{q}_s) = \frac{K_{\mathrm{arb}}}{k_{sz}} \iint d\boldsymbol{q}_i \, d\boldsymbol{\rho} \, V_p(\boldsymbol{\rho}) e^{-i(\boldsymbol{q}_p \cdot \boldsymbol{\rho} - \phi_0)}$$
$$\times e^{i(\Delta k_z - \Delta \bar{k}_z/2)L} \left[\frac{\sinh \Gamma(\Delta \bar{k}_z, \boldsymbol{\rho})L}{\Gamma(\Delta \bar{k}_z, \boldsymbol{\rho})} \right]$$
$$\times [T \, e^{i\gamma} A_i^*(\boldsymbol{q}_i, 0) f(L) + \sqrt{1 - T^2} \, B_i^*(\boldsymbol{q}_i, 0)].$$
$$(37b)$$

The above fields overlap at the beamsplitter to yield the field $A_s(\boldsymbol{q}_s) = \{A_{s1}(\boldsymbol{q}_s) + A_{s2}(\boldsymbol{q}_s)\}/\sqrt{2}$, and the measured intensity at the CCD camera takes the form

$$\langle |A_s(\boldsymbol{q}_s)|^2 \rangle = \frac{K_{\mathrm{arb}}}{k_{sz}^2} \int d\boldsymbol{\rho} \, \langle |V_p(\boldsymbol{\rho})|^2 \rangle \left| \frac{\sinh \Gamma(\Delta \bar{k}_z, \boldsymbol{\rho})L}{\Gamma(\Delta \bar{k}_z, \boldsymbol{\rho})} \right|^2$$
$$\times [1 + \bar{T}^2 |f(L)|^2 + 2 \bar{T} \, |f(L)|$$
$$\times \cos\{\arg f(L) + \bar{\gamma} + \phi_0\} + (1 - \bar{T}^2)]. \quad (38)$$

As seen in the above expression, when $|f(L)| \gg 1$, the terms quadratic in $\bar{T}$ do not cancel, and as a result, the visibility $V(\boldsymbol{q}_s)$ is *not* linear in $\bar{T}$.

We numerically study the effect of increasing pump strength on the spatial interference. For simplicity, we now assume the object is no longer structured, but has a uniform transmittance T, and compute the behavior of the visibility for increasing pump strengths. We assume collinear
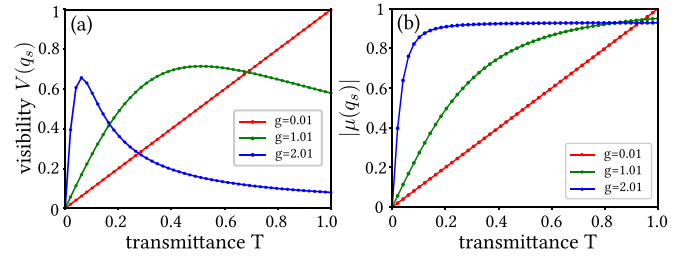

FIG. 11. (a) Depicts the interference visibility, and (b) depicts the degree of coherence $|\mu(\boldsymbol{q}_s)|$ as a function of object transmittance T for different pump amplitudes g (in arb units).

degenerate SPDC with the same parameters chosen in Sec. III A. In Fig. 11(a), we depict the visibility with respect to transmittance for different pump strengths g computed by numerically varying ϕ_0 from 0 to 2π in Eq. (38). While the visibility has a linear dependence on transmittance for $g = 0.01$ in the low-gain regime, the dependence is in general neither linear nor monotonic for $g = 1.01$ and $g = 2.01$ that correspond to the high-gain regime. The latter fact may be understood as follows: For $T = 0$, the fields $A_{s1}(\boldsymbol{q}_s)$ and $A_{s2}(\boldsymbol{q}_s)$ are equal in magnitude, but have no mutual coherence, and consequently, the visibility vanishes. However, for $T > 0$, the visibility increases with respect to T until some critical value, but when the classical "vacuum" seeding the second crystal is stronger than that seeding the first crystal, the field $A_{s2}(\boldsymbol{q}_s)$ is stronger than the field $A_{s1}(\boldsymbol{q}_s)$, which causes the visibility to decrease. This behavior of the visibility in the high-gain regime has also been predicted in existing quantum calculations for a monochromatic plane-wave pump [69–71].

At this juncture, one can ask whether the decline in visibility is only due to the disproportion of the overlapping fields $A_{s1}(\boldsymbol{q}_s)$ and $A_{s2}(\boldsymbol{q}_s)$ or whether there is also a simultaneous reduction in the degree of their mutual coherence. This question is important from a practical standpoint in the context of imaging because in the former case, the fields $A_{s1}(\boldsymbol{q}_s)$ and $A_{s2}(\boldsymbol{q}_s)$ can be equalized in magnitude by suitably attenuating $A_{s2}(\boldsymbol{q}_s)$ to realize perfect visibility [69,71], whereas in the latter case, the visibility cannot be optimized beyond $|\mu(\boldsymbol{q}_s)|$, where the mutual degree of coherence $\mu(\boldsymbol{q}_s)$ is defined as $\mu(\boldsymbol{q}_s) \equiv \langle A_{s1}^*(\boldsymbol{q}_s) A_{s2}(\boldsymbol{q}_s) \rangle / \sqrt{\langle A_{s1}(\boldsymbol{q}_s) A_{s1}^*(\boldsymbol{q}_s) \rangle \langle A_{s2}(\boldsymbol{q}_s) A_{s2}^*(\boldsymbol{q}_s) \rangle}$. Using Eqs. (37), we obtain

$$\mu(\boldsymbol{q}_s) = \frac{\int d\boldsymbol{\rho} \, \langle |V_p(\boldsymbol{\rho})|^2 \rangle |\, \Phi(\Delta \bar{k}_z, \boldsymbol{\rho}, L)|^2 \, f(L) \, \bar{T} \, e^{i\bar{\gamma}}}{\sqrt{\int d\boldsymbol{\rho} \, \langle |V_p(\boldsymbol{\rho})|^2 \rangle |\, \Phi(\Delta \bar{k}_z, \boldsymbol{\rho}, L)|^2} \sqrt{\int d\boldsymbol{\rho} \, \langle |V_p(\boldsymbol{\rho})|^2 \rangle |\, \Phi(\Delta \bar{k}_z, \boldsymbol{\rho}, L)|^2 \{1 + \bar{T}^2(|f(L)|^2 - 1)\}}}, \quad (39)$$

where $\Phi(\Delta \bar{k}_z, \boldsymbol{\rho}, L) \equiv \sinh \Gamma(\Delta \bar{k}_z, \boldsymbol{\rho}, L) / \Gamma(\Delta \bar{k}_z, \boldsymbol{\rho}, L)$. It may be verified that Eq. (39) is consistent with previous theoretical calculations for a monochromatic plane-wave pump [70,71]. We compute and plot the behavior of $|\mu(\boldsymbol{q}_s)|$ with respect to transmittance T in Fig. 11(b) for different pump amplitudes. In much similarity with the monochromatic plane-wave pump case [70,71], $|\mu(\boldsymbol{q}_s)|$ scales linearly with T for low gain, but the scaling does not remain linear for

increasing gain. Nevertheless, $\mu(\boldsymbol{q}_s)$ remains very high even for large gain, therefore allowing the possibility to realize imaging with high visibility by means of attenuation. There is a small discrepancy from perfect coherence in the high-gain regime for unity transmittance, i.e., $\mu(\boldsymbol{q}_s) < 1$ for $T = 1$. In fact, it is evident from Eq. (39) that owing to the explicit dependence of $f(L)$ on $\boldsymbol{\rho}$, in general $|\mu(\boldsymbol{q}_s)| \neq 1$ for $T = 1$. However, we are unable to ascertain if this discrepancy is a

genuine physical effect, or an artifact of the "narrow-band" approximation because the discrepancy vanishes for the monochromatic plane-wave pump case.

V. SUMMARY AND OUTLOOK

We describe a classical model that simulates SPDC as DFG of the pump field with a hypothetical stochastic field that mimics the effect of vacuum fluctuations. We show that the second-order spatiotemporal correlations of the field generated from DFG replicate those of the signal field from SPDC. In particular, for low gain, the second-order correlations predicted by the model are identical to those predicted by the quantum calculation of the reduced density matrix of the signal photon, whereas for high gain, we present experimental measurements of the far-field intensity profile, OAM spectrum, and the wavelength spectrum for increasing pump strengths and demonstrate their agreement with the model's predictions. The far-field intensity profile and wavelength spectrum exhibit broadening, whereas the OAM spectrum exhibits narrowing with increasing gain.

Next, we use the model to theoretically analyze second-order interference in SU(1,1) interferometers and induced coherence experiments. We derive analytical expressions for the second-order spatiotemporal correlations of the output field of a prototypical SU(1,1) interferometer, and illustrate some salient features of the interference in the spatial domain through numerical simulations. We then apply the model to the induced coherence experiment, and derive expressions for spatial interference in the low- and high-gain regimes. Interestingly, the model correctly predicts the experimentally-observed linear scaling of the visibility with object transmittance in the spontaneous low-gain limit—a feature that is often regarded as the quintessential signature of the nonclassicality of induced coherence. We then apply the model to numerically analyze the intriguing induced coherence-related phenomena known as "quantum imaging with undetected photons" [43] and "quantifying the momentum correlation between two light beams by detecting one" [73]. Finally, we analyze the behavior of visibility and degree of mutual coherence of the interfering fields in the high-gain regime for increasing pump strengths. We find the behavior to be consistent with previous studies that assumed a monochromatic plane-wave pump [70,71].

In the future, our paper may potentially pave the way towards a better understanding of the classical-quantum divide in the context of SPDC and induced coherence. The model itself could be viewed as a specific application of stochastic electrodynamics—a broader research program that attempts to explain a variety of quantum electrodynamic phenomena by positing the existence of a classical stochastic background radiation field that statistically mimics the zero-point vacuum fluctuations [77–81]. It may be possible to push the model further to investigate higher-order correlations and other effects related to SPDC, SU(1,1) interference, and induced coherence, which could potentially shed light on the limits to which classical physics can be used to approximate the quantum world. In this context, we note that an important artefact of the present model is that it assumes the existence of a classical "vacuum" only in the idler channel, which breaks the signal-idler symmetry that is inherent in Eqs. (4) and the full quantum-mechanical picture of SPDC. But it may be possible to derive an analogous classical model that retains the signal-idler symmetry by assuming the existence of classical "vacuum" fields in both, the signal and idler channels, and it would be interesting to explore if such a symmetric classical model might be able to predict additional phenomena that are beyond the purview of the present model.

In addition to fundamental implications, our paper may also have significant practical applicability. Our model can be a useful theoretical tool for analyzing high-gain SPDC [30,31,55,61] and induced coherence experiments [43,73,74]. Moreover, using the connection between Schmidt decomposition in quantum theory and the coherent-mode decomposition in classical coherence theory [34,56], our model can be used to extract important properties of the global quantum state such as the Schmidt spectrum and Schmidt modes [82]. A precise knowledge of these properties may not only lead to a better quantitative understanding of high-dimensional multiphoton entanglement of the high-gain SPDC field [83], but may also inform experiments aimed at harnessing the underlying correlations for applications in imaging [18,19], quantum state preparation [20], phase metrology [60], radiation shaping [61], microscopy [62], sensing [64], and spectroscopy [68].

APPENDIX A: DERIVATION OF THE DFG EQUATIONS

Upon substituting Eqs. (1) and (3) into (2), we obtain

$$\left[\nabla^2 + \frac{n_j^2 \omega_j^2}{c^2} \right] \int d\boldsymbol{q}_j A_j(\boldsymbol{q}_j, \omega_j, z) e^{i(\boldsymbol{q}_j \cdot \boldsymbol{\rho} + k_{jz} z)} = -\frac{4 d_{\text{eff}} \omega_j^2}{c^2} \iiint d\omega_p \, d\boldsymbol{q}_p \, d\boldsymbol{q}_l A_p(\boldsymbol{q}_p, \omega_p) A_l^*(\boldsymbol{q}_l, \omega_l, z) e^{i[(\boldsymbol{q}_p - \boldsymbol{q}_l) \cdot \boldsymbol{\rho} + (k_{pz} - k_{lz}) z]},$$

(A1)

for $j = s(i)$ and $l = i(s)$. We first focus only on the left-hand side of the above equation. Using $\nabla \equiv (\nabla_\perp, \partial/\partial z)$ and $|\boldsymbol{k}_j| = n_j\omega_j/c = \sqrt{|\boldsymbol{q}_j|^2 + k_{jz}^2}$ and simplifying, we obtain

$$
\int d\boldsymbol{q}_j (|\boldsymbol{k}_j|^2 - |\boldsymbol{q}_j|^2) A_j(\boldsymbol{q}_j, \omega_j, z) e^{i(\boldsymbol{q}_j \cdot \boldsymbol{\rho} + k_{jz}z)} + \frac{\partial}{\partial z} \int d\boldsymbol{q}_j \left[\frac{\partial A_j(\boldsymbol{q}_j, \omega_j, z)}{\partial z} + ik_{jz} A_j(\boldsymbol{q}_j, \omega_j, z) \right] e^{i(\boldsymbol{q}_j \cdot \boldsymbol{\rho} + k_{jz}z)}
$$

$$
= \int d\boldsymbol{q}_j \left\{ k_{jz}^2 A_j(\boldsymbol{q}_j, \omega_j, z) e^{i(\boldsymbol{q}_j \cdot \boldsymbol{\rho} + k_{jz}z)} + \left[\frac{\partial^2 A_j(\boldsymbol{q}_j, \omega_j, z)}{\partial z^2} + 2ik_{jz} \frac{\partial A_j(\boldsymbol{q}_j, \omega_j, z)}{\partial z} - k_{jz}^2 A_j(\boldsymbol{q}_j, \omega_j, z) \right] e^{i(\boldsymbol{q}_j \cdot \boldsymbol{\rho} + k_{jz}z)} \right\}.
$$

We make the slowly-varying envelope approximation $\frac{\partial^2}{\partial z^2} A_j(\boldsymbol{q}_j, \omega_j, z) \ll k_{jz} \frac{\partial}{\partial z} A_j(\boldsymbol{q}_j, \omega_j, z)$, use a different dummy variable $\boldsymbol{q}_j'$ instead of $\boldsymbol{q}_j$, and equate to the right-hand side of Eq. (A1) to obtain

$$
\int d\boldsymbol{q}_j' \, 2ik_{jz}' \frac{\partial A_j(\boldsymbol{q}_j', \omega_j, z)}{\partial z} e^{i(\boldsymbol{q}_j' \cdot \boldsymbol{\rho} + k_{jz}'z)} = -\frac{4d_{\text{eff}}\omega_j^2}{c^2} \iiint d\omega_p \, d\boldsymbol{q}_p \, d\boldsymbol{q}_l \, A_p(\boldsymbol{q}_p, \omega_p) A_l^*(\boldsymbol{q}_l, \omega_l, z) e^{i[(\boldsymbol{q}_p - \boldsymbol{q}_l)\cdot\boldsymbol{\rho} + (k_{pz} - k_{lz})z]}.
$$

Multiplying both sides by $e^{-i\boldsymbol{q}_j \cdot \boldsymbol{\rho}}$ and integrating with respect to $\boldsymbol{\rho}$ over the transverse extent of the crystal, we obtain

$$
\iint d\boldsymbol{\rho} \, d\boldsymbol{q}_j' \, 2ik_{jz}' \frac{\partial A_j(\boldsymbol{q}_j', \omega_j, z)}{\partial z} e^{i[(\boldsymbol{q}_j' - \boldsymbol{q}_j)\cdot\boldsymbol{\rho} + k_{jz}'z]}
$$

$$
= -\frac{4d_{\text{eff}}\omega_j^2}{c^2} \int d\boldsymbol{\rho} \iiint d\omega_p \, d\boldsymbol{q}_p \, d\boldsymbol{q}_l \, A_p(\boldsymbol{q}_p, \omega_p) A_l^*(\boldsymbol{q}_l, \omega_l, z) e^{i[(\boldsymbol{q}_p - \boldsymbol{q}_l - \boldsymbol{q}_j)\cdot\boldsymbol{\rho} + (k_{pz} - k_{lz})z]}.
$$

We now assume that the transverse extent of the crystal is much larger than the pump spot-size and therefore, the integration over $\boldsymbol{\rho}$ can be performed over the entire infinite range of $\boldsymbol{\rho}$ to yield

$$
\int d\boldsymbol{q}_j' \, 2ik_{jz}' \frac{\partial A_j(\boldsymbol{q}_j', \omega_j, z)}{\partial z} e^{ik_{jz}'z} \delta(\boldsymbol{q}_j' - \boldsymbol{q}_j) = -\frac{4d_{\text{eff}}\omega_j^2}{c^2} \iiint d\omega_p \, d\boldsymbol{q}_p \, d\boldsymbol{q}_l \, A_p(\boldsymbol{q}_p, \omega_p) A_l^*(\boldsymbol{q}_l, \omega_l, z) e^{i(k_{pz} - k_{lz})z} \delta(\boldsymbol{q}_p - \boldsymbol{q}_l - \boldsymbol{q}_j),
$$

where the Dirac delta relation on the right-hand side expresses conservation of transverse momentum, i.e., $\boldsymbol{q}_p = \boldsymbol{q}_s + \boldsymbol{q}_i$. Using $\omega_p = \omega_s + \omega_i$ and $\Delta k_z = k_{pz} - k_{sz} - k_{iz}$, the above equation can be simplified to yield

$$
\frac{\partial A_j(\boldsymbol{q}_j, \omega_j, z)}{\partial z} = \frac{2id_{\text{eff}}\omega_j^2}{k_{jz}c^2} \iint d\omega_l \, d\boldsymbol{q}_l \, A_p(\boldsymbol{q}_p, \omega_p) A_l^*(\boldsymbol{q}_l, \omega_l, z) e^{i\Delta k_z z},
$$

which represents Eq. (4a) for $(j, l) = (s, i)$, and Eq. (4b) for $(j, l) = (i, s)$ upon complex conjugation.

APPENDIX B: DETAILED CALCULATIONS FOR THE HIGH-GAIN REGIME

1. Derivation of the second-order differential equation (12) for the signal field

Upon substituting Eq. (10) into Eqs. (4), we obtain

$$
\frac{\partial A_s(\boldsymbol{q}_s, \omega_s, z)}{\partial z} = \frac{2id_{\text{eff}}\omega_s^2}{(2\pi)^3 k_{sz}c^2} \iiiint d\omega_i \, d\boldsymbol{q}_i \, d\boldsymbol{\rho} \, dt \, V_p(\boldsymbol{\rho}, t) \, e^{-i(\boldsymbol{q}_p \cdot \boldsymbol{\rho} - \omega_p t)} A_i^*(\boldsymbol{q}_i, \omega_i, z) e^{i\Delta k_z z}, \tag{B1a}
$$

$$
\frac{\partial A_i^*(\boldsymbol{q}_i, \omega_i, z)}{\partial z} = \frac{-2id_{\text{eff}}\omega_i^2}{(2\pi)^3 k_{iz}c^2} \iiiint d\omega_s \, d\boldsymbol{q}_s \, d\boldsymbol{\rho} \, dt \, V_p^*(\boldsymbol{\rho}, t) \, e^{i(\boldsymbol{q}_p \cdot \boldsymbol{\rho} - \omega_p t)} A_s(\boldsymbol{q}_s, \omega_s, z) e^{-i\Delta k_z z}. \tag{B1b}
$$

We now consider the right-hand side of Eq. (11)

$$
\frac{2id_{\text{eff}}\omega_s^2}{(2\pi)^3 k_{sz}c^2} \iiiint d\omega_i \, d\boldsymbol{q}_i \, d\boldsymbol{\rho} \, dt \, V_p(\boldsymbol{\rho}, t) e^{-i(\boldsymbol{q}_p \cdot \boldsymbol{\rho} - \omega_p t)} e^{i\Delta k_z z} \left[\frac{\partial A_i^*(\boldsymbol{q}_i, \omega_i, z)}{\partial z} + i\Delta k_z A_i^*(\boldsymbol{q}_i, \omega_i, z) \right]
$$

$$
= \frac{4d_{\text{eff}}^2\omega_s^2\bar{\omega}_i^2}{(2\pi)^6 k_{sz}\bar{k}_{iz}c^4} \iiiint d\omega_i \, d\boldsymbol{q}_i \, d\boldsymbol{\rho} \, dt \iiiint d\omega_s' \, d\boldsymbol{q}_s' \, d\boldsymbol{\rho}' \, dt' V_p(\boldsymbol{\rho}, t) V_p^*(\boldsymbol{\rho}', t') e^{-i[(\boldsymbol{q}_p \cdot \boldsymbol{\rho} - \boldsymbol{q}_p' \cdot \boldsymbol{\rho}') - (\omega_p t - \omega_p' t')]} A_s(\boldsymbol{q}_s', \omega_s', z)
$$

$$
\times e^{i(\Delta k_z - \Delta k_z')z} + i\Delta\bar{k}_z \frac{2id_{\text{eff}}\omega_s^2}{(2\pi)^3 k_{sz}c^2} \iiiint d\omega_i \, d\boldsymbol{q}_i \, d\boldsymbol{\rho} \, dt \, V_p(\boldsymbol{\rho}, t) \, e^{-i(\boldsymbol{q}_p \cdot \boldsymbol{\rho} - \omega_p t)} A_i^*(\boldsymbol{q}_i, \omega_i, z) e^{i\Delta k_z z}
$$

$$
= \frac{4d_{\text{eff}}^2\omega_s^2\bar{\omega}_i^2}{(2\pi)^6 k_{sz}\bar{k}_{iz}c^4} \iiiint d\omega_i \, d\boldsymbol{q}_i \, d\boldsymbol{\rho} \, dt \iiiint d\omega_s' \, d\boldsymbol{q}_s' \, d\boldsymbol{\rho}' \, dt' V_p(\boldsymbol{\rho}, t) V_p^*(\boldsymbol{\rho}', t') e^{-i[(\boldsymbol{q}_s \cdot \boldsymbol{\rho} - \boldsymbol{q}_s' \cdot \boldsymbol{\rho}') - (\omega_s t - \omega_s' t') + \boldsymbol{q}_i(\boldsymbol{\rho} - \boldsymbol{\rho}') - \omega_i(t - t')]}
$$

$$
\times A_s(\boldsymbol{q}_s', \omega_s', z) e^{i(\Delta k_z - \Delta k_z')z} + i\Delta\bar{k}_z \frac{\partial A_s(\boldsymbol{q}_s, \omega_s, z)}{\partial z}
$$

$$\begin{aligned}
&= \frac{4d_{\mathrm{eff}}^2 \omega_s^2 \bar{\omega}_i^2}{(2\pi)^3 k_{sz} \bar{k}_{iz} c^4} \iint d\boldsymbol{\rho}\, dt \iiiint d\omega_s'\, d\boldsymbol{q}_s'\, d\boldsymbol{\rho}'\, dt' V_p(\boldsymbol{\rho},t) V_p^*(\boldsymbol{\rho}',t') e^{-i[(\boldsymbol{q}_s\cdot\boldsymbol{\rho}-\boldsymbol{q}_s'\cdot\boldsymbol{\rho}')-(\omega_s t-\omega_s' t')]} \delta(\boldsymbol{\rho}-\boldsymbol{\rho}')\delta(t-t') A_s(\boldsymbol{q}_s',\omega_s',z) \\
&\quad \times e^{i(\Delta k_z - \Delta k_z')z} + i\Delta \bar{k}_z \frac{\partial A_s(\boldsymbol{q}_s,\omega_s,z)}{\partial z} \\
&= \frac{4d_{\mathrm{eff}}^2 \omega_s^2 \bar{\omega}_i^2}{(2\pi)^3 k_{sz} \bar{k}_{iz} c^4} \iint d\boldsymbol{\rho}\, dt \iint d\omega_s'\, d\boldsymbol{q}_s' |V_p(\boldsymbol{\rho},t)|^2 e^{-i[(\boldsymbol{q}_s-\boldsymbol{q}_s')\cdot\boldsymbol{\rho}-(\omega_s-\omega_s)t]} A_s(\boldsymbol{q}_s',\omega_s',z)\, e^{i(\Delta k_z - \Delta k_z')z} + i\Delta \bar{k}_z \frac{\partial A_s(\boldsymbol{q}_s,\omega_s,z)}{\partial z} \\
&= \frac{4d_{\mathrm{eff}}^2 \omega_s^2 \bar{\omega}_i^2}{k_{sz} \bar{k}_{iz} c^4} |V_p(\boldsymbol{\rho},t)|^2 \iint d\omega_s'\, d\boldsymbol{q}_s'\, \delta(\boldsymbol{q}_s-\boldsymbol{q}_s')\,\delta(\omega_s-\omega_s)\, A_s(\boldsymbol{q}_s',\omega_s',z)\, e^{i(\Delta k_z - \Delta k_z')z} + i\Delta \bar{k}_z \frac{\partial A_s(\boldsymbol{q}_s,\omega_s,z)}{\partial z} \\
&= \frac{4d_{\mathrm{eff}}^2 \omega_s^2 \bar{\omega}_i^2}{k_{sz} \bar{k}_{iz} c^4} |V_p(\boldsymbol{\rho},t)|^2 A_s(\boldsymbol{q}_s,\omega_s,z) + i\Delta \bar{k}_z \frac{\partial A_s(\boldsymbol{q}_s,\omega_s,z)}{\partial z}.
\end{aligned}$$

We note that in the second-last step of the above calculation, we have used the fact that the pump intensity profile $|V_p(\boldsymbol{\rho},t)|^2$ has a very slow variation with respect to $\boldsymbol{\rho}$ and t due to our assumption that the frequency and angular bandwidth of the pump is much smaller than that of the generated field. Consequently, the function $|V_p(\boldsymbol{\rho},t)|^2$ could be taken out of the integral. Upon shifting the above result to the left-hand side of Eq. (11), we obtain Eq. (12).

2. Solution of the second-order differential equation (12) for the signal field

Substituting an ansatz solution of the form $A_s(\boldsymbol{q}_s,\omega_s,z) = e^{rz}$ into Eq. (12), we obtain $r^2 - i\Delta \bar{k}_z r - \bar{G}^2(\boldsymbol{\rho},t) = 0$, which has the roots $r_\pm = i\Delta \bar{k}_z/2 \pm \Gamma(\Delta \bar{k}_z,\boldsymbol{\rho},t)$, where $\Gamma(\Delta \bar{k}_z,\boldsymbol{\rho},t)$ is defined by Eq. (15). The general solution then takes the form $A_s(\boldsymbol{q}_s,\omega_s,z) = C e^{r_+ z} + D e^{r_- z}$, where C and D are scaling factors to be determined by initial conditions. The first condition $A_s(\boldsymbol{q}_s,\omega_s,z=0) = 0$ implies $C + D = 0$, and the value of $\partial A_s(\boldsymbol{q}_s,\omega_s,z)/\partial z|_{z=0}$ obtained by evaluating Eq. (B1a) for $z=0$ yields

$$C = \frac{i d_{\mathrm{eff}} \omega_s^2}{(2\pi)^3 k_{sz} c^2} \iiiint d\omega_i\, d\boldsymbol{q}_i\, d\boldsymbol{\rho}\, dt\, \frac{V_p(\boldsymbol{\rho},t)}{\Gamma(\Delta \bar{k}_z,\boldsymbol{\rho},t)}\, e^{-i(\boldsymbol{q}_p\cdot\boldsymbol{\rho}-\omega_p t)} A_i^*(\boldsymbol{q}_i,\omega_i,0).$$

We again use the approximation that the function $\Gamma(\Delta \bar{k}_z,\boldsymbol{\rho},t)$ from its dependence on $|V_p(\boldsymbol{\rho},t)|^2$ has a very slow variation with respect to $\boldsymbol{\rho}$ and t. The above relation then implies $A_s(\boldsymbol{q}_s,\omega_s,z) = 2C\, e^{i\Delta \bar{k}_z z/2} \sinh[\Gamma(\Delta \bar{k}_z,\boldsymbol{\rho},t)z]$, which yields Eq. (14) for $z = L$.

3. Evaluating the high-gain spatiotemporal correlation function of the signal field

Using Eq. (14), we evaluate

$$\begin{aligned}
\langle A_s(\boldsymbol{q}_s,\omega_s,z) A_s^*(\boldsymbol{q}_s',\omega_s',z) \rangle &= \frac{4d_{\mathrm{eff}}^2 \omega_s^2 \omega_s'^2}{(2\pi)^6 k_{sz} k_{sz}' c^4} \iiiint d\omega_i\, d\boldsymbol{q}_i\, d\boldsymbol{\rho}\, dt \iiiint d\omega_i'\, d\boldsymbol{q}_i'\, d\boldsymbol{\rho}'\, dt' \langle V_p(\boldsymbol{\rho},t) V_p(\boldsymbol{\rho}',t') \rangle \\
&\quad \times e^{-i[(\boldsymbol{q}_p\cdot\boldsymbol{\rho}-\boldsymbol{q}_p'\cdot\boldsymbol{\rho}')-(\omega_p t-\omega_p' t')]} \langle A_i^*(\boldsymbol{q}_i,\omega_i,0) A_i(\boldsymbol{q}_i',\omega_i',0) \rangle \left[\frac{\sinh\Gamma(\Delta \bar{k}_z,\boldsymbol{\rho},t)L}{\Gamma(\Delta \bar{k}_z,\boldsymbol{\rho},t)} \right] \left[\frac{\sinh\Gamma(\Delta \bar{k}_z',\boldsymbol{\rho}',t')L}{\Gamma(\Delta \bar{k}_z',\boldsymbol{\rho}',t')} \right] e^{i[(\Delta k_z - \Delta k_z')+(\Delta \bar{k}_z - \Delta \bar{k}_z')/2]L} \\
&= \frac{4d_{\mathrm{eff}}^2 \omega_s^2 \omega_s'^2}{(2\pi)^6 k_{sz} k_{sz}' c^4} \iiiint d\omega_i\, d\boldsymbol{q}_i\, d\boldsymbol{\rho}\, dt \iiiint d\omega_i'\, d\boldsymbol{q}_i'\, d\boldsymbol{\rho}'\, dt' \langle V_p(\boldsymbol{\rho},t) V_p(\boldsymbol{\rho}',t') \rangle\, e^{-i[(\boldsymbol{q}_p\cdot\boldsymbol{\rho}-\boldsymbol{q}_p'\cdot\boldsymbol{\rho}')-(\omega_p t-\omega_p' t')]} \\
&\quad \times \frac{\hbar\omega_i}{8\pi\epsilon_0} \delta(\boldsymbol{q}_i-\boldsymbol{q}_i')\delta(\omega_i-\omega_i') \left[\frac{\sinh\Gamma(\Delta \bar{k}_z,\boldsymbol{\rho},t)L}{\Gamma(\Delta \bar{k}_z,\boldsymbol{\rho},t)} \right] \left[\frac{\sinh\Gamma(\Delta \bar{k}_z',\boldsymbol{\rho}',t')L}{\Gamma(\Delta \bar{k}_z',\boldsymbol{\rho}',t')} \right] e^{i[(\Delta k_z - \Delta k_z')+(\Delta \bar{k}_z - \Delta \bar{k}_z')/2]L} \\
&= \frac{4d_{\mathrm{eff}}^2 \omega_s^2 \omega_s'^2}{(2\pi)^6 k_{sz} k_{sz}' c^4} \iiiint d\omega_i\, d\boldsymbol{q}_i\, d\boldsymbol{\rho}\, dt\, \frac{\hbar\omega_i}{8\pi\epsilon_0} \iint d\boldsymbol{\rho}'\, dt' \langle V_p(\boldsymbol{\rho},t) V_p(\boldsymbol{\rho}',t') \rangle\, e^{-i[(\boldsymbol{q}_s\cdot\boldsymbol{\rho}-\boldsymbol{q}_s'\cdot\boldsymbol{\rho}')-(\omega_s t-\omega_s' t')]} e^{i[\boldsymbol{q}_i\cdot(\boldsymbol{\rho}-\boldsymbol{\rho}')-\omega_i(t-t')]} \\
&\quad \times \left[\frac{\sinh\Gamma(\Delta \bar{k}_z,\boldsymbol{\rho},t)L}{\Gamma(\Delta \bar{k}_z,\boldsymbol{\rho},t)} \right] \left[\frac{\sinh\Gamma(\Delta \bar{k}_z',\boldsymbol{\rho}',t')L}{\Gamma(\Delta \bar{k}_z',\boldsymbol{\rho}',t')} \right] e^{i[(\Delta k_z - \Delta k_z')+(\Delta \bar{k}_z - \Delta \bar{k}_z')/2]L} \\
&= \frac{\hbar\omega_{i0} d_{\mathrm{eff}}^2 \omega_s^2 \omega_s'^2}{(2\pi)^4 \epsilon_0 k_{sz} k_{sz}' c^4} \iint d\boldsymbol{\rho}\, dt \iint d\boldsymbol{\rho}'\, dt' \langle V_p(\boldsymbol{\rho},t) V_p(\boldsymbol{\rho}',t') \rangle\, e^{-i[(\boldsymbol{q}_s\cdot\boldsymbol{\rho}-\boldsymbol{q}_s'\cdot\boldsymbol{\rho}')-(\omega_s t-\omega_s' t')]} \delta(\boldsymbol{\rho}-\boldsymbol{\rho}')\delta(t-t') \\
&\quad \times \left[\frac{\sinh\Gamma(\Delta \bar{k}_z,\boldsymbol{\rho},t)L}{\Gamma(\Delta \bar{k}_z,\boldsymbol{\rho},t)} \right] \left[\frac{\sinh\Gamma(\Delta \bar{k}_z',\boldsymbol{\rho}',t')L}{\Gamma(\Delta \bar{k}_z',\boldsymbol{\rho}',t')} \right] e^{i(\Delta \bar{k}_z - \Delta \bar{k}_z')L/2} \\
&= \frac{\hbar\omega_{i0} d_{\mathrm{eff}}^2 \omega_s^2 \omega_s'^2}{(2\pi)^4 \epsilon_0 k_{sz} k_{sz}' c^4} \iint d\boldsymbol{\rho}\, dt\, \langle |V_p(\boldsymbol{\rho},t)|^2 \rangle\, e^{-i[(\boldsymbol{q}_s-\boldsymbol{q}_s')\cdot\boldsymbol{\rho}-(\omega_s-\omega_s')t]} \left[\frac{\sinh\Gamma(\Delta \bar{k}_z,\boldsymbol{\rho},t)L}{\Gamma(\Delta \bar{k}_z,\boldsymbol{\rho},t)} \right] \left[\frac{\sinh\Gamma(\Delta \bar{k}_z',\boldsymbol{\rho},t)L}{\Gamma(\Delta \bar{k}_z',\boldsymbol{\rho},t)} \right] e^{i(\Delta \bar{k}_z - \Delta \bar{k}_z')L/2},
\end{aligned}$$

which is Eq. (16).

4. Evaluating the output field from the SU(1,1) setup

As the field $A_s(\boldsymbol{q}_s, \omega_s, z')$ satisfies Eq. (12), we can assume an ansatz solution of the form $A_s(\boldsymbol{q}_s, \omega_s, z') = Ce^{r_+ z'} + De^{r_- z'}$, where $r_\pm = i\Delta\bar{k}_z/2 \pm \Gamma(\Delta\bar{k}_z, \boldsymbol{\rho}, t)$. Thus, we have $C + D = A_s(\boldsymbol{q}_s, \omega_s, z' = 0)$ and $Cr_+ + Dr_- = \dot{A}_s(\boldsymbol{q}_s, \omega_s, z' = 0) = \partial A_s(\boldsymbol{q}_s, \omega_s, z')/\partial z|_{z'=0}$, which implies $C = \{\dot{A}_s(\boldsymbol{q}_s, \omega_s, z' = 0) - r_- A_s(\boldsymbol{q}_s, \omega_s, z' = 0)\}/(r_+ - r_-)$ and $D = \{r_+ A_s(\boldsymbol{q}_s, \omega_s, z' = 0) - \dot{A}_s(\boldsymbol{q}_s, \omega_s, z' = 0)\}/(r_+ - r_-)$. Substituting from Eqs. (14) and (26), we obtain

$$A_s(\boldsymbol{q}_s, \omega_s, z' = L) = \frac{2id_{\text{eff}}\omega_s^2}{(2\pi)^3 k_{sz}c^2} \iiint\int d\omega_i\, d\boldsymbol{q}_i\, d\boldsymbol{\rho}\, dt\, V_p(\boldsymbol{\rho}, t)\, e^{-i(\boldsymbol{q}_p\cdot\boldsymbol{\rho} - \omega_p t)} A_i^*(\boldsymbol{q}_i, \omega_i, 0)\, e^{i(\Delta k_z - \Delta\bar{k}_z/2)L}$$

$$\times \left\{ e^{\Gamma L}\left[\frac{e^{i\Delta k_z^{(\text{air})}D}}{2\Gamma}\left\{ \cosh\Gamma L + \frac{i\Delta\bar{k}_z}{2\Gamma}\sinh\Gamma L \right\} + \{\Gamma - i\Delta\bar{k}_z/2\}\frac{\sinh\Gamma L}{2\Gamma^2} \right]\right.$$

$$\left. + e^{-\Gamma L}\left[\{i\Delta\bar{k}_z/2 + \Gamma\}\frac{\sinh\Gamma L}{2\Gamma^2} - \frac{e^{i\Delta k_z^{(\text{air})}D}}{2\Gamma}\left\{ \cosh\Gamma L + \frac{i\Delta\bar{k}_z}{2\Gamma}\sinh\Gamma L \right\} \right]\right\}$$

$$= \frac{2id_{\text{eff}}\omega_s^2}{(2\pi)^3 k_{sz}c^2} \iiint\int d\omega_i\, d\boldsymbol{q}_i\, d\boldsymbol{\rho}\, dt\, V_p(\boldsymbol{\rho}, t)\, e^{-i(\boldsymbol{q}_p\cdot\boldsymbol{\rho} - \omega_p t)} A_i^*(\boldsymbol{q}_i, \omega_i, 0)\, e^{i(\Delta k_z - \Delta\bar{k}_z/2)L}$$

$$\times \left\{ e^{i\Delta k_z^{(\text{air})}D}\left\{ \frac{\sinh 2\Gamma L}{2\Gamma} + \frac{i\Delta\bar{k}_z}{2\Gamma^2}\sinh^2\Gamma L \right\} + \frac{\sinh\Gamma L}{2\Gamma^2}(2\Gamma\cosh\Gamma L - i\Delta\bar{k}_z\sinh\Gamma L) \right\}$$

$$= \frac{2id_{\text{eff}}\omega_s^2}{(2\pi)^3 k_{sz}c^2} \iiint\int d\omega_i\, d\boldsymbol{q}_i\, d\boldsymbol{\rho}\, dt\, V_p(\boldsymbol{\rho}, t)\, e^{-i(\boldsymbol{q}_p\cdot\boldsymbol{\rho} - \omega_p t)} A_i^*(\boldsymbol{q}_i, \omega_i, 0)\, e^{i(\Delta k_z - \Delta\bar{k}_z/2)L}$$

$$\times \left\{ \frac{\sinh 2\Gamma L}{2\Gamma}\left(1 + e^{i\Delta k_z^{(\text{air})}D}\right) - \frac{i\Delta\bar{k}_z}{2}\left(\frac{\sinh\Gamma L}{\Gamma}\right)^2\left(1 - e^{i\Delta k_z^{(\text{air})}D}\right) \right\}$$

$$= \frac{2id_{\text{eff}}\omega_s^2}{(2\pi)^3 k_{sz}c^2} \iiint\int d\omega_i\, d\boldsymbol{q}_i\, d\boldsymbol{\rho}\, dt\, V_p(\boldsymbol{\rho}, t)\, e^{-i(\boldsymbol{q}_p\cdot\boldsymbol{\rho} - \omega_p t)} A_i^*(\boldsymbol{q}_i, \omega_i, 0)\, e^{i(\Delta k_z - \Delta\bar{k}_z/2)L}\, e^{i\Delta k_z^{(\text{air})}D/2}$$

$$\times \left\{ \frac{\sinh 2\Gamma L}{\Gamma}\cos\left\{\Delta k_z^{(\text{air})}D/2\right\} - \Delta\bar{k}_z\left(\frac{\sinh\Gamma L}{\Gamma}\right)^2\sin\left\{\Delta k_z^{(\text{air})}D/2\right\} \right\}$$

$$= \frac{4id_{\text{eff}}\omega_s^2}{(2\pi)^3 k_{sz}c^2} \iiint\int d\omega_i\, d\boldsymbol{q}_i\, d\boldsymbol{\rho}\, dt\, V_p(\boldsymbol{\rho}, t)\, e^{-i(\boldsymbol{q}_p\cdot\boldsymbol{\rho} - \omega_p t)} A_i^*(\boldsymbol{q}_i, \omega_i, 0)\, e^{i(\Delta k_z - \Delta\bar{k}_z/2)L}\, e^{i\Delta k_z^{(\text{air})}D/2}\left(\frac{\sinh\Gamma L}{\Gamma}\right)$$

$$\times \left[\cosh\Gamma L\,\cos\left\{\Delta k_z^{(\text{air})}D/2\right\} - \frac{\Delta\bar{k}_z}{2\Gamma}\sinh\Gamma L\,\sin\left\{\Delta k_z^{(\text{air})}D/2\right\} \right],$$

which is Eq. (32).

---

[1] D. Klyshko, Coherent photon decay in a nonlinear medium, JETP Lett. **6**, 490 (1967).

[2] D. C. Burnham and D. L. Weinberg, Observation of Simultaneity in Parametric Production of Optical Photon Pairs, Phys. Rev. Lett. **25**, 84 (1970).

[3] R. W. Boyd, *Nonlinear Optics* (Academic Press, New York, 2020).

[4] C. Couteau, Spontaneous parametric down-conversion, Contemp. Phys. **59**, 291 (2018).

[5] D. N. Klyshko, *Photons and Nonlinear Optics* (Gordon and Breach Science Publishers, New York, 1988).

[6] C. K. Hong and L. Mandel, Theory of parametric frequency down conversion of light, Phys. Rev. A **31**, 2409 (1985).

[7] T. E. Keller and M. H. Rubin, Theory of two-photon entanglement for spontaneous parametric down-conversion driven by a narrow pump pulse, Phys. Rev. A **56**, 1534 (1997).

[8] W. P. Grice and I. A. Walmsley, Spectral information and distinguishability in type-II down-conversion with a broadband pump, Phys. Rev. A **56**, 1627 (1997).

[9] C. K. Hong, Z. Y. Ou, and L. Mandel, Measurement of Subpicosecond Time Intervals Between Two Photons by Interference, Phys. Rev. Lett. **59**, 2044 (1987).

[10] Y. H. Shih and C. O. Alley, New Type of Einstein-Podolsky-Rosen-Bohm Experiment Using Pairs of Light Quanta Produced by Optical Parametric Down Conversion, Phys. Rev. Lett. **61**, 2921 (1988).

[11] X. Y. Zou, L. J. Wang, and L. Mandel, Induced Coherence and Indistinguishability in Optical Interference, Phys. Rev. Lett. **67**, 318 (1991).

[12] G. Weihs, T. Jennewein, C. Simon, H. Weinfurter, and A. Zeilinger, Violation of Bell's Inequality Under Strict Einstein Locality Conditions, Phys. Rev. Lett. **81**, 5039 (1998).

[13] D. Bouwmeester, J.-W. Pan, K. Mattle, M. Eibl, H. Weinfurter, and A. Zeilinger, Experimental quantum teleportation, Nature (London) **390**, 575 (1997).

[14] T. Jennewein, C. Simon, G. Weihs, H. Weinfurter, and A. Zeilinger, Quantum Cryptography with Entangled Photons, Phys. Rev. Lett. **84**, 4729 (2000).

[15] P.-A. Moreau, E. Toninelli, T. Gregory, and M. J. Padgett, Imaging with quantum states of light, Nat. Rev. Phys. **1**, 367 (2019).

[16] E. Brambilla, A. Gatti, M. Bache, and L. A. Lugiato, Simultaneous near-field and far-field spatial quantum correlations in the high-gain regime of parametric down-conversion, Phys. Rev. A **69**, 023802 (2004).

[17] I. N. Agafonov, M. V. Chekhova, and G. Leuchs, Two-color bright squeezed vacuum, Phys. Rev. A **82**, 011801(R) (2010).

[18] O. Jedrkiewicz, Y.-K. Jiang, E. Brambilla, A. Gatti, M. Bache, L. A. Lugiato, and P. Di Trapani, Detection of Sub-Shot-Noise Spatial Correlation in High-Gain Parametric Down Conversion, Phys. Rev. Lett. **93**, 243601 (2004).

[19] G. Brida, M. Genovese, and I. Ruo Berchera, Experimental realization of sub-shot-noise quantum imaging, Nat. Photonics **4**, 227 (2010).

[20] G. Harder, T. J. Bartley, A. E. Lita, S. W. Nam, T. Gerrits, and C. Silberhorn, Single-Mode Parametric-Down-Conversion States with 50 Photons as a Source for Mesoscopic Quantum Optics, Phys. Rev. Lett. **116**, 143601 (2016).

[21] T. S. Iskhakov, I. N. Agafonov, M. V. Chekhova, and G. Leuchs, Polarization-Entangled Light Pulses of 10^5 Photons, Phys. Rev. Lett. **109**, 150502 (2012).

[22] A. M. Brańczyk, T. M. Stace, and T. C. Ralph, Time ordering in spontaneous parametric down-conversion, AIP Conf. Proc. **1363**, 335 (2011).

[23] N. Quesada and J. E. Sipe, Effects of time ordering in quantum nonlinear optics, Phys. Rev. A **90**, 063840 (2014).

[24] S. L. Braunstein, Squeezing as an irreducible resource, Phys. Rev. A **71**, 055801 (2005).

[25] B. Dayan, Theory of two-photon interactions with broadband down-converted light and entangled photons, Phys. Rev. A **76**, 043813 (2007).

[26] W. Wasilewski, A. I. Lvovsky, K. Banaszek, and C. Radzewicz, Pulsed squeezed light: Simultaneous squeezing of multiple modes, Phys. Rev. A **73**, 063819 (2006).

[27] N. Quesada, G. Triginer, M. D. Vidrighin, and J. E. Sipe, Theory of high-gain twin-beam generation in waveguides: From Maxwell's equations to efficient simulation, Phys. Rev. A **102**, 033519 (2020).

[28] A. Christ, K. Laiho, A. Eckstein, K. N. Cassemiro, and C. Silberhorn, Probing multimode squeezing with correlation functions, New J. Phys. **13**, 033027 (2011).

[29] P. Sharapova, A. M. Pérez, O. V. Tikhonova, and M. V. Chekhova, Schmidt modes in the angular spectrum of bright squeezed vacuum, Phys. Rev. A **91**, 043816 (2015).

[30] K. Y. Spasibko, T. S. Iskhakov, and M. V. Chekhova, Spectral properties of high-gain parametric down-conversion, Opt. Express **20**, 7507 (2012).

[31] P. R. Sharapova, G. Frascella, M. Riabinin, A. M. Pérez, O. V. Tikhonova, S. Lemieux, R. W. Boyd, G. Leuchs, and M. V. Chekhova, Properties of bright squeezed vacuum at increasing brightness, Phys. Rev. Research **2**, 013371 (2020).

[32] S. Mrówczyński and B. Müller, Wigner functional approach to quantum field dynamics, Phys. Rev. D **50**, 7542 (1994).

[33] F. S. Roux, Parametric down-conversion beyond the semiclassical approximation, Phys. Rev. Research **2**, 033398 (2020).

[34] H. Di Lorenzo Pires, F. M. G. J. Coppens, and M. P. van Exter, Type-I spontaneous parametric down-conversion with a strongly focused pump, Phys. Rev. A **83**, 033837 (2011).

[35] W. H. Louisell, A. Yariv, and A. E. Siegman, Quantum fluctuations and noise in parametric processes. I., Phys. Rev. **124**, 1646 (1961).

[36] B. Schröder, Optical parametric amplification from quantum noise, Opt. Quantum Electron. **15**, 57 (1983).

[37] A. Gatti, H. Wiedemann, L. A. Lugiato, I. Marzoli, G.-L. Oppo, and S. M. Barnett, Langevin treatment of quantum fluctuations and optical patterns in optical parametric oscillators below threshold, Phys. Rev. A **56**, 877 (1997).

[38] S. Trajtenberg-Mills, A. Karnieli, N. Voloch-Bloch, E. Megidish, H. S. Eisenberg, and A. Arie, Simulating correlations of structured spontaneously down-converted photon pairs, Laser Photonics Rev. **14**, 1900321 (2020).

[39] P. Di Trapani, G. Valiulis, W. Chinaglia, and A. Andreoni, Two-Dimensional Spatial Solitary Waves from Traveling-Wave Parametric Amplification of the Quantum Noise, Phys. Rev. Lett. **80**, 265 (1998).

[40] A. Picozzi and M. Haelterman, Influence of walk-off, dispersion, and diffraction on the coherence of parametric fluorescence, Phys. Rev. E **63**, 056611 (2001).

[41] B. Yurke, S. L. McCall, and J. R. Klauder, SU(2) and SU(1,1) interferometers, Phys. Rev. A **33**, 4033 (1986).

[42] D. Klyshko, Ramsey interference in two-photon parametric scattering, Zh. Eksp. Teor. Fiz. **104**, 2676 (1993) [JETP Lett. **104**, 2676 (1993)].

[43] G. B. Lemos, V. Borish, G. D. Cole, S. Ramelow, R. Lapkiewicz, and A. Zeilinger, Quantum imaging with undetected photons, Nature (London) **512**, 409 (2014).

[44] L. Mandel and E. Wolf, *Optical Coherence and Quantum Optics* (Cambridge University Press, Cambridge, 1995).

[45] Z. J. Ou, *Quantum Optics for Experimentalists* (World Scientific, Singapore, 2017).

[46] The factor of 2 on the left-hand side arises because both $\langle A_i(\boldsymbol{q}_i', \omega_i', 0) A_i^*(\boldsymbol{q}_i, \omega_i, 0)\rangle$ and $\langle A_i^*(\boldsymbol{q}_i', \omega_i', 0) A_i(\boldsymbol{q}_i, \omega_i, 0)\rangle$ contribute equally to the energy density, whereas on the right-hand side, only $\langle \text{vac}|\hat{a}_i(\boldsymbol{q}_i', \omega_i') \hat{a}_i^\dagger(\boldsymbol{q}_i, \omega_i)|\text{vac}\rangle$ contributes because $\langle \text{vac}|\hat{a}_i^\dagger(\boldsymbol{q}_i', \omega_i') \hat{a}_i(\boldsymbol{q}_i, \omega_i)|\text{vac}\rangle = 0$. See Sec. 8.12 of Ref. [47] for details.

[47] P. W. Milonni, *The Quantum Vacuum An Introduction to Quantum Electrodynamics* (Academic Press, 2013).

[48] R. J. Glauber, The quantum theory of optical coherence, Phys. Rev. **130**, 2529 (1963).

[49] It is also possible to derive the spectral density of vacuum within the program of stochastic electrodynamics in a purely classical manner from considerations of translational, rotational, and Lorentz invariance. We refer the interested reader to Ref. [77] for a semitechnical account, and Ref. [79] for the actual derivation.

[50] A. L. Grimsmo and A. Blais, Squeezing and quantum state engineering with Josephson travelling wave amplifiers, npj Quantum Inf. **3**, 20 (2017).

[51] V. A. Averchenko, G. Frascella, M. Kalash, A. Cavanna, and M. V. Chekhova, Reconstructing two-dimensional spatial

modes for classical and quantum light, Phys. Rev. A **102**, 053725 (2020).

[52] S. Walborn, C. Monken, S. Pádua, and P. S. Ribeiro, Spatial correlations in parametric down-conversion, Phys. Rep. **495**, 87 (2010).

[53] D. Eimerl, L. Davis, S. Velsko, E. K. Graham, and A. Zalkin, Optical, mechanical, and thermal properties of barium borate, J. Appl. Phys. **62**, 1968 (1987).

[54] A. Mair, A. Vaziri, G. Weihs, and A. Zeilinger, Entanglement of the orbital angular momentum states of photons, Nature (London) **412**, 313 (2001).

[55] L. Beltran, G. Frascella, A. M. Perez, R. Fickler, P. R. Sharapova, M. Manceau, O. V. Tikhonova, R. W. Boyd, G. Leuchs, and M. V. Chekhova, Orbital angular momentum modes of high-gain parametric down-conversion, J. Opt. **19**, 044005 (2017).

[56] G. Kulkarni, R. Sahu, O. S. Magaña-Loaiza, R. W. Boyd, and A. K. Jha, Single-shot measurement of the orbital-angular-momentum spectrum of light, Nat. Commun. **8**, 1054 (2017).

[57] A. K. Jha, G. S. Agarwal, and R. W. Boyd, Partial angular coherence and the angular schmidt spectrum of entangled two-photon fields, Phys. Rev. A **84**, 063847 (2011).

[58] We have implicitly assumed that the pump field is a transform-limited Gaussian pulse, which is not strictly true. However, for our purposes, this assumption will not introduce significant errors.

[59] M. V. Chekhova and Z. Y. Ou, Nonlinear interferometers in quantum optics, Adv. Opt. Photonics **8**, 104 (2016).

[60] M. Manceau, G. Leuchs, F. Khalili, and M. Chekhova, Detection Loss Tolerant Supersensitive Phase Measurement with an SU(1,1) Interferometer, Phys. Rev. Lett. **119**, 223604 (2017).

[61] S. Lemieux, M. Manceau, P. R. Sharapova, O. V. Tikhonova, R. W. Boyd, G. Leuchs, and M. V. Chekhova, Engineering the Frequency Spectrum of Bright Squeezed Vacuum via Group Velocity Dispersion in an SU(1,1) Interferometer, Phys. Rev. Lett. **117**, 183601 (2016).

[62] A. V. Paterova, S. M. Maniam, H. Yang, G. Grenci, and L. A. Krivitsky, Hyperspectral infrared microscopy with visible light, Sci. Adv. **6**, eabd0460 (2020).

[63] G. J. Machado, G. Frascella, J. P. Torres, and M. V. Chekhova, Optical coherence tomography with a nonlinear interferometer in the high parametric gain regime, Appl. Phys. Lett. **117**, 094002 (2020).

[64] M. Kutas, B. Haase, P. Bickert, F. Riexinger, D. Molter, and G. von Freymann, Terahertz quantum sensing, Sci. Adv. **6**, eaaz8065 (2020).

[65] P. E. Ciddor, Refractive index of air: New equations for the visible and near infrared, Appl. Opt. **35**, 1566 (1996).

[66] A. M. Pérez, T. S. Iskhakov, P. Sharapova, S. Lemieux, O. V. Tikhonova, M. V. Chekhova, and G. Leuchs, Bright squeezed-vacuum source with 1.1 spatial mode, Opt. Lett. **39**, 2403 (2014).

[67] L. J. Wang, X. Y. Zou, and L. Mandel, Induced coherence without induced emission, Phys. Rev. A **44**, 4614 (1991).

[68] D. A. Kalashnikov, A. V. Paterova, S. P. Kulik, and L. A. Krivitsky, Infrared spectroscopy with visible light, Nat. Photonics **10**, 98 (2016).

[69] A. Belinsky and D. Klyshko, Interference of classical and non-classical light, Phys. Lett. A **166**, 303 (1992).

[70] H. Wiseman and K. Mølmer, Induced coherence with and without induced emission, Phys. Lett. A **270**, 245 (2000).

[71] M. I. Kolobov, E. Giese, S. Lemieux, R. Fickler, and R. W. Boyd, Controlling induced coherence for quantum imaging, J. Opt. **19**, 054003 (2017).

[72] M. Lahiri, A. Hochrainer, R. Lapkiewicz, G. B. Lemos, and A. Zeilinger, Nonclassicality of induced coherence without induced emission, Phys. Rev. A **100**, 053839 (2019).

[73] A. Hochrainer, M. Lahiri, R. Lapkiewicz, G. B. Lemos, and A. Zeilinger, Quantifying the momentum correlation between two light beams by detecting one, Proc. Natl. Acad. Sci. USA **114**, 1508 (2017).

[74] A. Hochrainer, M. Lahiri, R. Lapkiewicz, G. B. Lemos, and A. Zeilinger, Interference fringes controlled by noninterfering photons, Optica **4**, 341 (2017).

[75] J. H. Shapiro, D. Venkatraman, and F. N. C. Wong, Classical imaging with undetected photons, Sci. Rep. **5**, 10329 (2015).

[76] A. C. Cardoso, L. P. Berruezo, D. F. Ávila, G. B. Lemos, W. M. Pimenta, C. H. Monken, P. L. Saldanha, and S. Pádua, Classical imaging with undetected light, Phys. Rev. A **97**, 033827 (2018).

[77] T. H. Boyer, The classical vacuum, Sci. Am. **253**, 70 (1985).

[78] T. W. Marshall, Random electrodynamics, Proc. R. Soc. London **276**, 475 (1963).

[79] T. H. Boyer, Classical statistical thermodynamics and electromagnetic zero-point radiation, Phys. Rev. **186**, 1304 (1969).

[80] T. H. Boyer, Random electrodynamics: The theory of classical electrodynamics with classical electromagnetic zero-point radiation, Phys. Rev. D **11**, 790 (1975).

[81] L. De la Peña and A. M. Cetto, *The Quantum Dice: An Introduction to Stochastic Electrodynamics* (Springer Science & Business Media, New York, 2013).

[82] S. S. Straupe, D. P. Ivanov, A. A. Kalinkin, I. B. Bobrov, and S. P. Kulik, Angular Schmidt modes in spontaneous parametric down-conversion, Phys. Rev. A **83**, 060302(R) (2011).

[83] B. Kanseri, T. Iskhakov, G. Rytikov, M. Chekhova, and G. Leuchs, Multiphoton nonclassical correlations in entangled squeezed vacuum states, Phys. Rev. A **87**, 032110 (2013).